


Structural controls on the localization of the mineralized Copper Cliff embayment and the Copper Cliff Offset dyke, Sudbury Igneous Complex, Canada

 The corrections made in this section will be reviewed and approved by a journal production editor.

 Lucie Mathieu^a, Ulrich Riller^b, Lisa Gibson^c, Peter Lightfoot^d

^aCentre d'études sur les Ressources minérales (CERM), Département des Sciences appliquées (DSA), Université du Québec à Chicoutimi (UQAC), 555 boul. de l'université, Chicoutimi, G7H 2B1 QC, Canada

^bInstitut für Geologie, Universität Hamburg, Bundesstraße 55, 20146 Hamburg, Germany

^cVale, North American Exploration, 337 Power St., Copper Cliff, Ontario, Canada

^dDepartment of Earth Sciences, University of Western Ontario, 1151 Richmond Street N., London, ON N6A 5B7, Canada

Abstract

The Main Mass of the Sudbury Igneous Complex (SIC) is a 1.5–5 km thick, layered sheet of impact melt rocks, intensely studied because of the magmatic Ni-Cu-PGE sulfide deposits associated with the base of the Main Mass and connected dykes, known as the Sublayer and Offset dykes, respectively. The mode of emplacement of the mineralized Offset dykes that connect to the Main Mass through morphologic crater-floor irregularities (embayments) and the style of post-cratering deformation that affected the Offset dykes is not fully understood. This field-based study of the Copper Cliff Embayment (CCE) and Offset (CCO) dyke contributes to unraveling the mode of melt emplacement and the role of pre-impact faults in the deformation of the southern SIC. Field relationships indicate that the CCO dyke formed before the CCE and Sublayer were chemically fully evolved. Respective melts were injected into footwall rocks weakened by pre-impact deformation and cratering as a protracted event, with barren quartz diorite (QD) emplaced prior to mineralized, inclusion-bearing quartz diorite (IQD). Massive sulfide ore bodies appear to have formed late in the evolution of the dyke and physical separation (decoupling) of silicate magma and sulfide melt is required. NW-SE-shortening folded and faulted the strata hosting the CCO dyke and deformation was facilitated through re-activated E-W-striking, pre-impact faults. Restoring the initial geometry of the dyke and embayment, using 3D modelling and field constraints, helped to refine total slip estimates along major faults and confirmed that melts migrated gravitationally downward into the CCO dyke.

Keywords: Sudbury Igneous Complex (SIC); Copper Cliff Offset dyke and Embayment; Magma; Fault reactivation; 3D model; Structural restoration

1 Introduction

The Sudbury Igneous Complex (SIC) is the 1.5–5 km thick layered sheet of impact melt rocks (Main Mass) of the 1.85 Ga Sudbury impact structure, Ontario, Canada (Grieve et al., 1991; Krogh et al., 1984; Lightfoot, 2017). The base of the melt sheet is distinguished from the Main Mass and comprises an inclusion-rich mineralized norite, termed the Sublayer. The Sublayer is distributed in funnel-shaped crater-floor depressions that served as entry points of radial dykes. These dykes are segmented by several post-cratering faults and are therefore known as Offset dykes (Grant and Bite, 1984). The Sublayer is associated with the contact type Ni-Cu-PGE ore bodies, while the Offset dykes contain almost 50% of the magmatic sulfide metals of the Sudbury mining camp (Lightfoot, 2017).

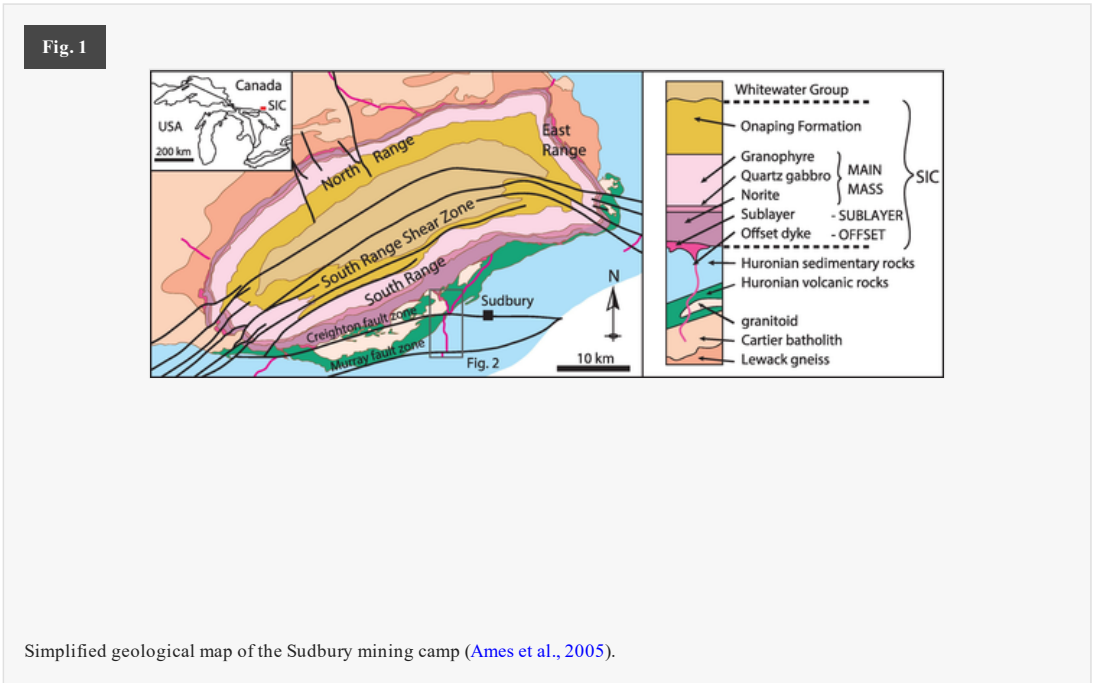
One of these dykes, the Copper Cliff Offset (CCO) dyke, contains several vertically elongated bodies of magmatic Ni-Cu massive sulfide deposits (Cochrane, 1984; Coleman, 1902; Collins, 1937; Grant and Bite, 1984; Lightfoot et al., 1997a; Pattison, 1979; Souch et al., 1969; Yates, 1938). The CCO and other Offset dykes may have been formed by one or several injection events during differentiation of the impact melt sheet (Lightfoot, 2017; Lightfoot and Farrow, 2002; Murphy and Spray, 2002; Pilles et al., 2018; Prevec and Cawthorn, 2002; Rousell and Brown, 2009; Wood and Spray, 1998). The mode of emplacement of the ore bodies is unclear; they may have been emplaced as pipe-shaped

bodies late in the formation of the dyke or as one initially continuous sulfide melt body that segmented during cooling and/or deformation of the dyke (Mourre, 2000; Scott and Benn, 2002).

The SIC was deformed by three successive orogenic events, which preserved a part of the melt sheet from erosion and induced folding and faulting (Clark and Riller, 2017; Clendenen et al., 1988; Cowan and Schwerdtner, 1994; Dreuse et al., 2010; Milkereit and Green, 1992). This field-based study focuses on the CCO dyke and on the Copper Cliff Embayment (CCE) that connects the CCO dyke to the Main Mass of the SIC. Using the Copper Cliff town area as an example, this study aims at understanding the development of embayments and Offset dykes at the base of the Main Mass of the SIC. This study also aims at unravelling the role of pre-impact faults in controlling the emplacement of the CCO dyke and the style of post-cratering deformation. This study has implications for exploration of the CCO dyke for magmatic sulfide mineralization.

2 Geological setting

The rocks described in this contribution were metamorphosed to greenschist facies.[Instruction: please add a space here (between 'facies' and 'but')]but the prefix ‘meta-’ is omitted throughout the manuscript. The Main Mass of the SIC formed by impact-induced melting of crustal rocks and assimilation of target rocks (Prevec, 2000), and separated into norite, gabbro, and granophyre layers (Fig. 1). These layers may result from either viscous emulsion differentiation of the impact melt sheet (Zieg and Marsh, 2005) or *in-situ* fractional crystallization (Grieve et al., 1991; Latypov et al., 2019; Lightfoot, 2017). The Sudbury impact structure comprises the SIC, an outer zone of fractured and brecciated ‘footwall’ rocks (Sudbury Breccia), a partially reworked fallback breccia (Onaping Formation), and post-impact sedimentary rocks that overlay Main Mass SIC (Whitewater Group; Fig. 1) (Grieve et al., 2010; Rousell, 1984).



The impact melt rocks comprise the layered sheet (Main Mass) and underlying units; i.e., Sublayer and Offset dykes (Fig. 1). The Sublayer is a discontinuous and mineralized, inclusion-rich so-called norite unit (Ames et al., 2005; Souch et al., 1969). This unit is made of quartz gabbro and monzogabbro (Table 1) and is more felsic than the traditional ‘norite’ nomenclature suggests (Therriault et al., 2002). The Sublayer unit fills small-scale troughs and funnel-shaped morphological depressions of the former crater floor (Lightfoot, 2017), such as the Copper Cliff Embayment (CCE), which are connected to radial Offset dykes; e.g., the Copper Cliff Offset (CCO) dyke (Fig. 2). The CCE is ~1.6 km wide and narrows southward to ~100 m, where it connects with the 9 km long, <100 m to 10 m thick, CCO dyke (Cochrane, 1984; Grant and Bite, 1984).

Table 1

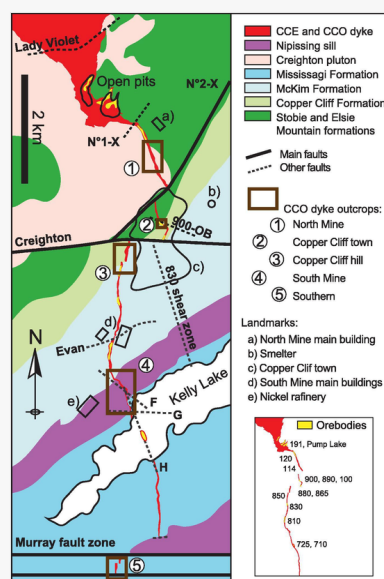
The table layout displayed in this section is not how it will appear in the final version. The representation below is solely purposed for providing corrections to the table. To preview the actual presentation of the table, please view the Proof.

Field designation of studied rocks and corresponding rock types.

Field designation		Rock type		
Historical	This contribution	Designation	Reference	
Sublayer	Norite	/	Quartz gabbro, monzogabbro	Thierriault et al. (2002)

CCE	Norite	Phases I, III, (IV) norite	Quartz monzodiorite	Capes (2001)
		phase II norite	gabbronorite	
		phases V and VI norite	quartz monzogabbronorite	
CCO dyke	Quartz diorite (QD)	QD-1 (sulphide- and inclusion-barren)	Granodiorite	Lightfoot et al. (1997a)
		QD-2 (some inclusions)		
		QD-3 (inclusions, Fig. 6a)		
	Inclusion-rich quartz diorite (IQD)	IQD-1 (sulphide, inclusion)		
		IQD-2 (sulphide-rich, inclusion)		
		IQD-3 (sulphide, inclusion-rich)		

Fig. 2



Geological map of the CCE and CCO dyke, displaying the main outcrops analyzed in detail and the location of sub-surface and underground ore bodies (Gordon and McDonald, 2015).

The CCE contains three types of rocks with gradational contacts (Table 1): 1) a quenched and discontinuous margin made of quartz monzodiorite; 2) an outer zone made of gabbronorite; and 3) quartz monzogabbronorite in the inner zone (Capes, 2001). The CCE was mostly made of two distinct types of melts with contrasting Al-contents, which may correspond to Sublayer melt contaminated by footwall rocks (Capes, 2001). The CCO dyke, in turn, is mostly made of granodiorite (Lightfoot et al., 1997a) and becomes more mafic southward (Grant and Bite, 1984). The rocks of the CCO dyke are referred to as the coarse-grained, inclusion-rich quartz diorite (IQD) and as the finer-grained, inclusion-poor quartz diorite (QD). The QD and IQD make up, respectively, the margin and the core (and locally the margin) of the Offset dykes (Cochrane, 1984; Grant and Bite, 1984). The CCO dyke also contains several pipe-shaped magmatic sulfide ore bodies located in the core (120, 100, 900 OB; Fig. 2) and along the eastern margin (830, 810, 800, 865, 880 OB) of the intrusion (Cochrane, 1984). The CCO dyke has a U-Pb zircon age of 1849.8 ± 2 Ma (Corfu and Lightfoot, 1996), which is within the range of high resolution ages available for the Main Mass, i.e., 1849.11 ± 0.19 Ma and 1849.53 ± 0.21 Ma (Davis, 2008). [Instruction: This sentence has been added to respond to a comment formulated by the external reviewer during the last round of review.]

The CCE and CCO dyke are in contact with the following footwall rocks: 1) granitoid rocks of the 2437 ± 2 Ma Creighton pluton (Bleeker et al., 2013); and 2) volcanic and sedimentary rocks of the ca. 2.45 Ga Huronian Supergroup (Card, 1978; Krogh et al., 1984). In the study area, the Huronian Supergroup is made of, from the oldest to youngest units: 1) mafic volcanic rocks of the Stobie and Elsie Mountain Formations (Elliot Lake Group); 2) felsic volcanic rocks of the Copper Cliff Formation; and 3) sandstones to turbidite successions of the McKim and Mississagi Formations (Fig. 2). The CCO dyke also intersects the 2.2–2.1 Ga Nipissing diabase sills (Buchan et al., 1989; Corfu and Andrews, 1986). These rocks have been deformed and metamorphosed by pre-impact deformation (Riller et al., 1999; Riller and Schwerdtner, 1997; Rousell and Long, 1998) that apparently re-activated normal faults into reverse faults; e.g., Murray and Creighton faults (Cochrane, 1984; Long, 2004; Zolnai et al., 1984). These faults were also re-activated by post-impact deformation related to the Yavapai-Mazatzal, Chieflakian-Pinawarian and Grenville orogenic events (Cochrane, 1984; Long, 2004; Zolnai et al., 1984).

The footwall rocks contain impact-generated pseudotachylite bodies referred to as Sudbury Breccia (Dressler, 1984; Riller et al., 2010b; Rousell et al., 2003; Speers, 1957; Thompson and Spray, 1994). Sudbury Breccia bodies generally consist of cm- to dm-thick elongate bodies but can develop broad belts of country rocks with intervals of Sudbury Breccia collectively up to 500 m wide; e.g., the South Range Breccia Belt – SRBB (Rousell et al., 2003; Scott and Spray, 2000). The Sudbury Breccia is derived from high-temperature melting, recrystallization and comminution of footwall lithologies, and it was partially transported into tensile fractures (O’Callaghan et al., 2016; Riller et al., 2010b).

Post-cratering events include metamorphism, folding and faulting related to the 1.7–1.6 Yavapai-Mazatzal, the 1.5–1.4 Ga Chieflakian-Pinvarian and the 1.2–1.0 Ga Grenville orogenies (Bailey et al., 2004; Papapavlou et al., 2018, 2017; Tschirhart and Morris, 2012). In the study area, the metamorphic facies reaches upper to mid-greenschist (Card, 1978; Fleet et al., 1987) and the crater floor has been tilted from sub-horizontal to 77°NW–45°NW (Dreuse et al., 2010; Grieve et al., 2008) during the folding and thrusting of the SIC (Clendenen et al., 1988; Cowan and Schwerdtner, 1994; Lenauer and Riller, 2017, 2012a, 2012b; Milkereit and Green, 1992; Santimano and Riller, 2012). Episodic deformation over a long period of time also formed the South Range Shear Zone (SRSZ), a NE-SW-striking brittle-ductile thrust fault located 2 km north of the CCE, which transported the southern SIC and adjacent footwall rocks toward the NW (Santimano and Riller, 2012; Shanks and Schwerdtner, 1991a). The CCO dyke is also intersected by mafic dykes (diabase) of the E-W-striking Trap dyke swarm, the 1.23 Ga NW-SE-striking Sudbury dyke swarm and of the 600–575 Ma E-W-striking Grenville dyke swarm (Bethune, 1997; Fahrig et al., 1986).

3 Methodology

3.1 Field data

This study relies on detailed mapping of the CCE and CCO dyke. Fieldwork was carried out during summers 2010 and 2011. The main outcropping areas are displayed in Fig. 2 and outcrops outlines can be found in a co-submission to *Data in Brief* (Mathieu et al. 2021) [Instruction: reference needed (this is the Data-in-brief accompanying publication - I don't know how to cite it)] [210—Data-in-Brief reference to add]. The CCE rocks are referred to as norite, even if the studied rocks contain more Si and K than typical norite. The IQD and QD designations are also used to refer to CCO rocks.

The studied SIC rocks contain a large amount (up to 30%) of xenoliths that can also be referred to as inclusions. The shape-preferred orientation (SPO) of the inclusions is studied in plan view following the method delineated by Launeau and Robin (1996). Inclusions are digitized from oriented field photographs and the SPO ellipses are computed. Results are provided as the dimensionless ratio a/b of the long over short axes of the ellipses. For strongly aligned inclusions, the a/b ratio is >1 , while a/b close to 1 corresponds to randomly oriented inclusions and/or to inclusions with circular sections in plan view.

A large amount of structural data, including orientations of quartz veins, fault planes (brittle and brittle-ductile faults) and associated slicken lines were measured in the field. Structural data are presented using strike and trend values restricted between azimuths of 000° and 180°. For example, an inclined NW-SE-striking plane that dips 30° toward the SW and a NE-SW-trending line dipping 40° toward the SW are referred to, respectively, as structures oriented 135/30 SW and 045/40 SW.

The percentage of dip-slip is calculated for each fault using the pitch angle. The kinematics of the faults is expressed as follows: 1) an oblique-slip fault that has accommodated reverse and dextral strike-slip movement is referred to as a dextral-reverse oblique-slip fault; and 2) faults that have accommodated $>80\%$ and $<30\%$ of dip-slip movement are referred to, respectively, as reverse and strike-slip faults. Field measurements, as well as rose diagrams, contour plots and Angelier diagrams can be found in a co-submission to *Data in Brief* (Mathieu et al. 2021) [0—reference to add] [Instruction: reference needed (this is the Data-in-brief accompanying publication - I don't know how to cite it)].

3.2 Three-dimensional (3D) model

The partner company, Vale, continuously updates a Datamine 3D model using exploration drill-cores and mine development data. To comment on the general geometry of the CCE and CCO dyke, a simplified 3D model was produced using the software Move (Midland Valley Ltd.). This 3D model is constrained by surface mapping, as well as 109 digitalized level plans of the Copper Cliff mine. Where the CCO dyke has not been mapped, the Datamine 3D model was used to fill the gaps. The maps located <100 vertical feet from each other were then combined to produce 19 simplified level plans. These plans were then digitized as curves using the software 2D-Move, and the curves were turned into surfaces using the software 3D-Move.

The 3D Move model comprises simplified surfaces that represent the CCO dyke, the CCE, a part of the crater floor, the main lithological contacts observed in footwall rocks, as well as the major faults that intersect the studied intrusion (Mathieu et al. 2021) [0—Data-in-Brief reference to add] [Instruction: reference needed (this is the Data-in-brief accompanying publication - I don't know how to cite it)]]. These surfaces extend from present erosion surface to the

4000 level (from the 250 m to the –970 m elevations). The (x, y, z) data of the 3D Move model are expressed in feet, using the company coordinate system of the Copper Cliff mine.

The major faults observed at surface and on the level plans are the N°1-X, N°2-X, 900-OB, F, G, Creighton and Evan faults, as well as the 830 shear zone (Fig. 2). The F and G faults are infiltrated by diabase dykes according to field observations. The Lady Violet fault, the northern and southern faults of the Murray fault zone and the H fault (South Mine outcrop) were modelled using field data only (Fig. 2). The 3D Move model was used to calculate the post-impact total slip magnitudes associated with the major faults, using the location of the CCO dyke on either side of the fault planes and a direction of movement deduced from the orientation of the slicken lines measured in the field (Table 2). For the N°1-X, 900-OB, F and G faults, slicken lines data are unavailable and were modelled assuming that the fault planes formed 30° (average fracture angle) from a sigma 1 vector oriented 135/00° (Table 2).

Table 2

i The table layout displayed in this section is not how it will appear in the final version. The representation below is solely purposed for providing corrections to the table. To preview the actual presentation of the table, please view the Proof.

General characteristics of the faults used to restore the 3D Move model.

Fault	Fault orientation	Slicken line orientation	Fault type	dip-slip	Source
Lady Violet	065/54 NW	171/53 NW	Sinistral-reverse	90%	Field data
N°2-X	045/55 NW	024/28 NE	Dextral-normal	40%	Field data
Creighton	090/75 N	103/40 NW	Dextral-reverse	45%	Field data
830 shear zone	165/60 SW	undetermined	Sinistral-normal	/	Field data
Evan	070/35 SE	136/33 SE	Dextral-reverse	70%	Field data
Murray	090/70 S	105/44 SE	Dextral-reverse	50%	Field data
N°1-X	025/42 NW	155/42 NW	Sinistral-reverse	65%	Model
900-OB	110/45 NE	122/12 NW	Sinistral strike-slip	20%	Model
Fault F	125/90°	125/00°	Dextral strike-slip	0	Model
Fault G	090/90°	090/00°	Sinistral strike-slip	0	Model

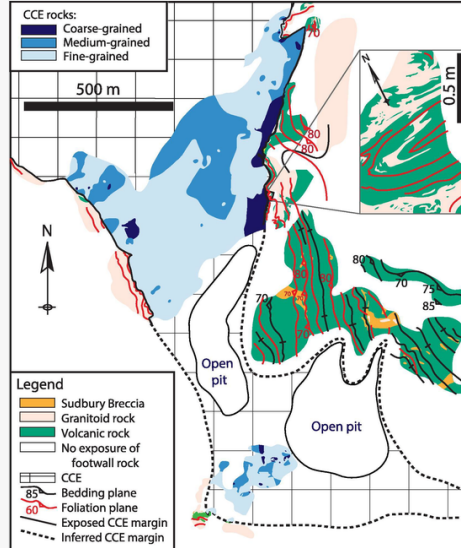
The 3D Move model was then restored sequentially, assuming that brittle deformation postdates ductile deformation; i.e., ‘un-faulting’ was performed before ‘un-folding’ in the software. The translation tools of the 3D-Move software attributes new (x, y, z) coordinates to each node of a surface without changing its shape. This tool was used to ‘un-fault’ the model using the mean total slip estimated for each fault (Table 2). ‘Un-folding’ was then performed using fold axes deduced from the general morphology of the CCE and CCO dyke (see below).

4 Results

4.1 Sublayer - footwall rock contacts

The CCE has a sharp and sub-vertical contact with Huronian basalts and granitoid rocks of the Creighton pluton that display, respectively, bedding planes and foliation planes defined by the shape-preferred alignment of feldspar and amphibole. These planes are sub-vertical, strike N-S to NW-SE and are gently to tightly folded within 5 m of the CCE contact (Fig. 3). The Sudbury Breccia bodies make up ~8% of the rocks in contact with the CCE.

Fig. 3



Geological map displaying the structure of footwall rocks and grain-size distribution in the CCE. The location of outcrops studied in detail is available in a co-submission to *Data in Brief* (Mathieu et al. 2021^[Instruction: reference needed (this is the Data-in-brief accompanying publication - I don't know how to cite it)]~~0 – Data in Brief~~^{Reference to add}).

The CCO dyke is sub-vertical, strikes NW-SE to N-S and its thickness decreases from 100 to 3 m from the northernmost to southernmost outcrop visited (Table 3). The CCO dyke intrudes the Creighton pluton near its eastern contact with the volcanic rocks of the Stobie Formation (North Mine outcrop; Fig. 2). This pre-impact lithological contact is decorated by Sudbury Breccia. The foliation planes of the footwall rocks are 170°-010° to NE-SW-striking sub-vertical planes that undulate gently (open folds; Fig. 4a). The CCO dyke is mostly sub-parallel to these planes. Locally, centimeter-thick ‘fingers’ of QD dissect the foliation planes.

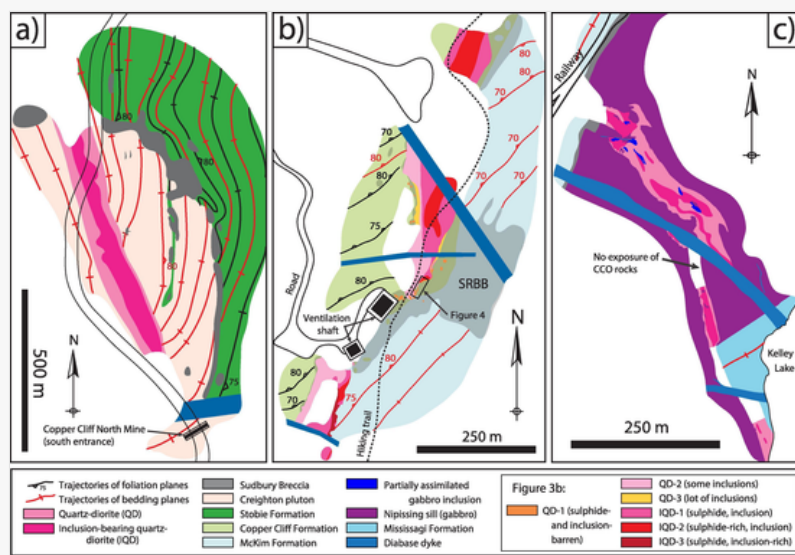
Table 3

i The table layout displayed in this section is not how it will appear in the final version. The representation below is solely purposed for providing corrections to the table. To preview the actual presentation of the table, please view the Proof.

Attitude of studied CCO dyke segments.

Outcrop	Strike	Thickness	Dyke morphology
North Mine	NNW-SSE	85–100 m	Linear contacts, IQD core and QD margins
Copper Cliff town	N-S to WNW-ESE	?	Poor quality outcrop (not described in the text)
Copper Cliff hill	NNW-SSW	85 m	Segmented dyke, both QD and IQD (several varieties) in the core and margins of the dyke
South Mine	NNW-SSE to NW-SE	13 to 45 m	Irregular contacts, IQD core and QD margins
Southern	N-S	3 to 20 m	Linear contacts, QD only

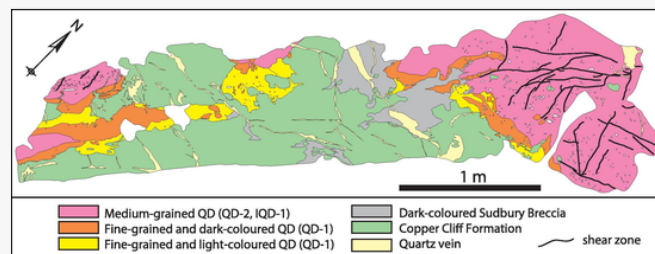
Fig. 4



Geological maps of the CCO dyke observed on the North Mine (a), Copper Cliff hill (b) and South Mine (c) outcrops. In these areas, the footwall rocks are 1–5 m thick lava flows interbedded with sandstone horizons (Stobie Formation), thinly bedded sandstones (McKim Formation) and coarse-grained porphyritic gabbro (Nipissing sill). On the Copper Cliff hill outcrop (b), the QD rocks are barren of sulfide and have the following characteristics: QD-1 is barren of inclusions; QD-2 contains up to 1% of 1 cm long rounded inclusions; and QD-3 contains 15–30% of cm to dm-long inclusions. The IQD rocks, on this outcrop, contain 2–6% of 1 cm long inclusions and <5% disseminated sulfide mineralization (IQD-1), are sulfide-rich (5–10% sulfide; IQD-2), or contain sulfide and 15–30% of dm-long angular to rounded sandstone and volcanic rock inclusions (IQD-3). The acronym SRBB stands for ‘South Range Breccia Belt’.

On the Copper Cliff hill outcrop (Fig. 2), the CCO dyke is located within 5 m of the contact between the McKim Formation (sandstones with bedding planes oriented 050/80 NW) and the Copper Cliff Formation (felsic volcanic rocks with foliation planes oriented 065/85 NW; Fig. 4b). The CCO dyke - footwall rocks contact is sharp and irregular (Figs. 4 and 5a). The CCO dyke is segmented where it intersects the SRBB (Fig. 4b and 5) and 10–50 cm patches of CCO melt rock are observed in the SRBB, up to 10 m from the contact of the CCO dyke (Fig. 5b).

Fig. 5



Geological map of the contact between the CCO dyke, the Copper Cliff Formation and the Sudbury Breccia (see Fig. 4b for location and for a description of QD-1, QD-2 and IQD-1).

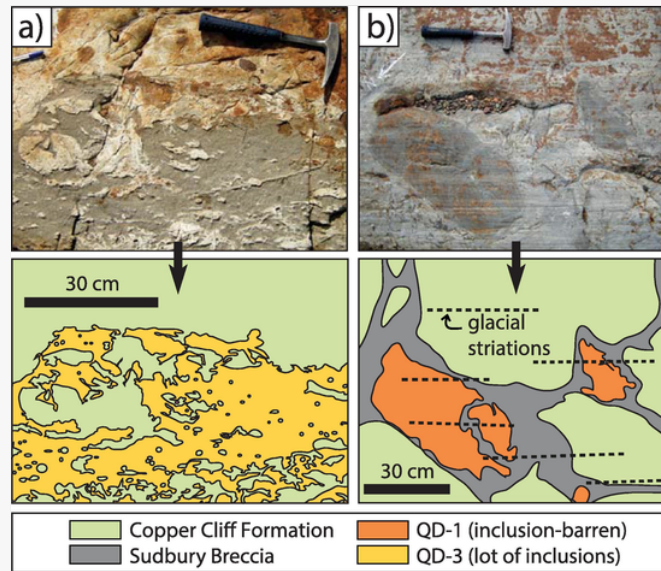
On the South Mine outcrop (Fig. 2), the CCO dyke is in contact with a Nipissing gabbro sill intruded in sandstone of the McKim Formation (Fig. 4c). The gabbro - sandstone contact strikes NE-SW and is overprinted by Sudbury Breccia. This contact is also displaced on either side of the dyke, indicating that the CCO dyke exploited a pre-existing NNW-SSE-striking structure (Fig. 4c). The CCO dyke - gabbro contact is sharp, angular and irregular. The dyke is thinner (3 to 20 m thick) on the southern outcrop, where it is in contact with sandstone of the Mississagi Formation. The CCO dyke is orthogonal to the subvertical and E-W-striking bedding planes in the sandstone. The CCO dyke - sandstone contact is straight to irregular.

4.2 Geology of the CCE

The CCE is made of medium- to coarse-grained (from <1 mm to >1 mm) noritic to dioritic rocks. Grain-size distribution is heterogeneous, as rocks tend to be coarser-grained in the core and along the eastern margin of the CCE (Fig. 3). These rocks are dominated by plagioclase, quartz (felsic minerals), as well as amphibole and biotite (mafic minerals) that grew during metamorphism at the expense of pyroxene and feldspar. The rocks are equigranular or contain porphyroblasts of biotite and were classified into phases I to VI on the basis of their texture and mafic to felsic mineral proportions (Fig. 7a; Table 1). Phases I to VI were not necessarily emplaced in this order and contain from 80% (phase I) to 20% (phase VI) of felsic minerals (Fig. 7a). Phases V and II represent 60% and 30%, respectively, of the outcropping surface of the CCE. Phase II is mostly observed along the western margin of the CCE, whereas phase V

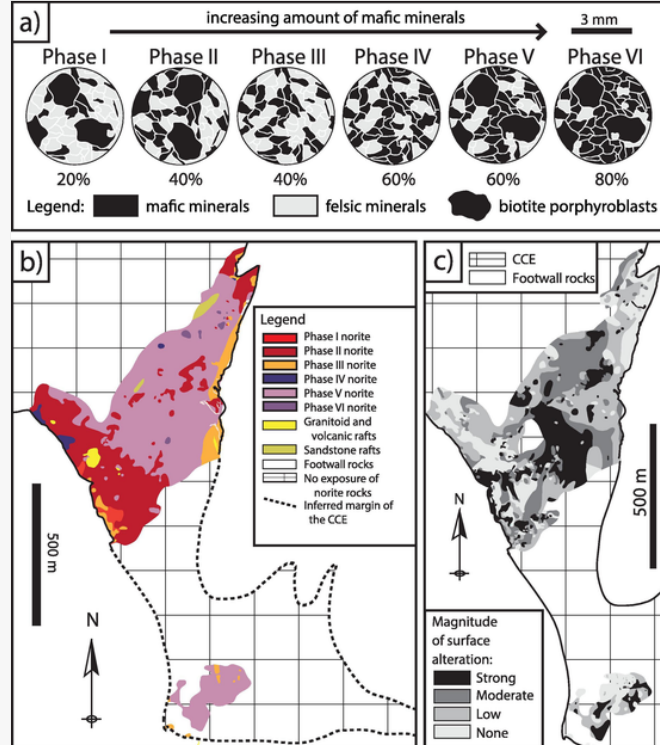
dominates the eastern half and western margin of the CCE (Fig. 7b), indicating that the core of the CCE is more mafic than its margin.

Fig. 6



Photographs and respective line drawings of the Copper Cliff hill outcrop; (a) contact between the Copper Cliff Formation and QD rocks (QD-3, see Fig. 4b for explanation); (b) fine-grained QD patches (QD-1) in the matrix of Sudbury Breccia (SRBB).

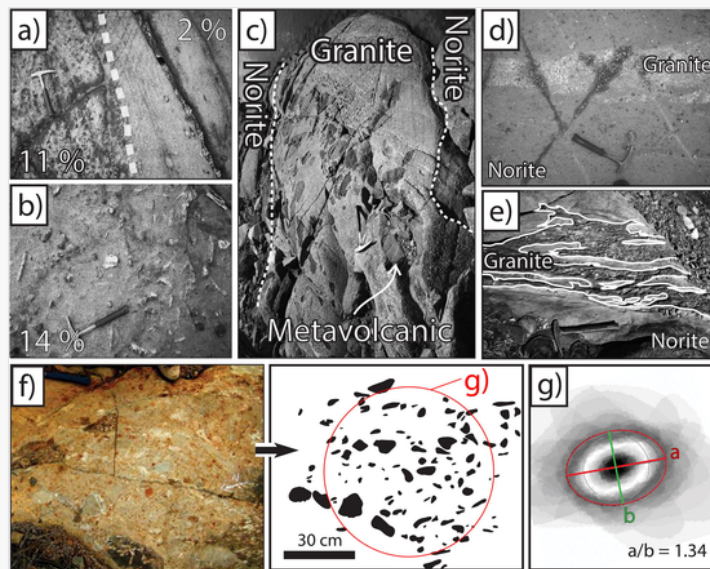
Fig. 7



(a) sketches of phases I to VI (so-called norite) observed in the CCE, with average proportion (%) of mafic minerals (biotite porphyroblasts excepted) observed in each phase; (b) distribution of phases I to VI and rafts in the CCE; (c) weathering intensity (rust) in the CCE, which is a proxy for sulfide content.

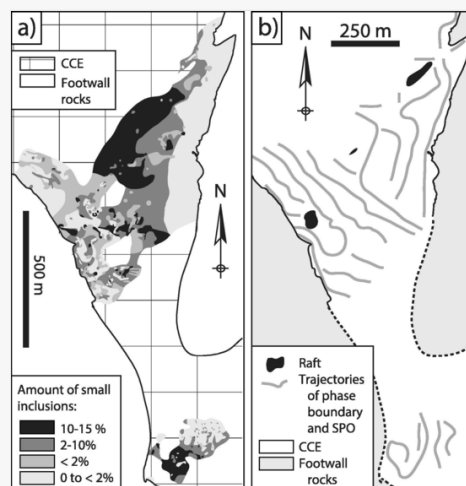
The CCE also contains disseminated to semi-massive sulfide mineralization. Sulfide proportion was estimated visually using the extent of surface weathering (Fig. 7c). Sulfide distribution is heterogeneous at a small scale, and there is a tendency for the proportion of sulfides to increase toward the core of the CCE (Fig. 7c). The CCE also contains a large amount of small inclusions (<10 cm long), large inclusions (10 s of cm long) and some meters-long rafts. The contact between phases with contrasting inclusion contents is sharp (Fig. 8a) and can be easily mapped in outcrop (Fig. 9a).

Fig. 8



Outcrop photographs of CCE (a–e) and CCO (f–g) rocks; (a) norite with 11% of small inclusions in sharp contact with an inclusion-poor norite; (b) norite with 14% of small inclusions; (c) large volcanic clast-bearing granitoid inclusion; (d) partially assimilated granitoid inclusion in norite; (e) stretched large granitoid inclusion in norite; (f) photograph and sketch of a sulfide- and inclusion-bearing IQD phase (IQD-3, see Fig. 4b for explanation); (g) result of a shape-preferred orientation (SPO) analysis carried on inclusions drawn from photograph (f).

Fig. 9



Maps of the CCE; (a) distribution of small inclusions (<10 cm long) in the CCE; (b) hand-drawn trajectories of maximum diameters of magmatic minerals and inclusions inferred from SPO analyses. These trajectories indicate that the CCE melt flowed southward and toward the CCO dyke.

The small inclusions (5% of the surface of the CCE) are rounded, have sharp contacts with the norite and are made of granitoid rock, volcanic rock and sandstone (Fig. 8b). The large inclusions are made of granitoid rock (80% of the inclusions) and basalt (20%). Contacts with the norite are diffuse to sharply defined. Six of the granitoid inclusions are curvi-planar, 1–2 m wide, 10 s of meters long, strike N–W to NW–SE and may contain angular volcanic inclusions (Fig. 7c–e). These inclusions are footwall inclusions (granitoid and volcanic rocks) heated and deformed by melt movement inside the CCE.

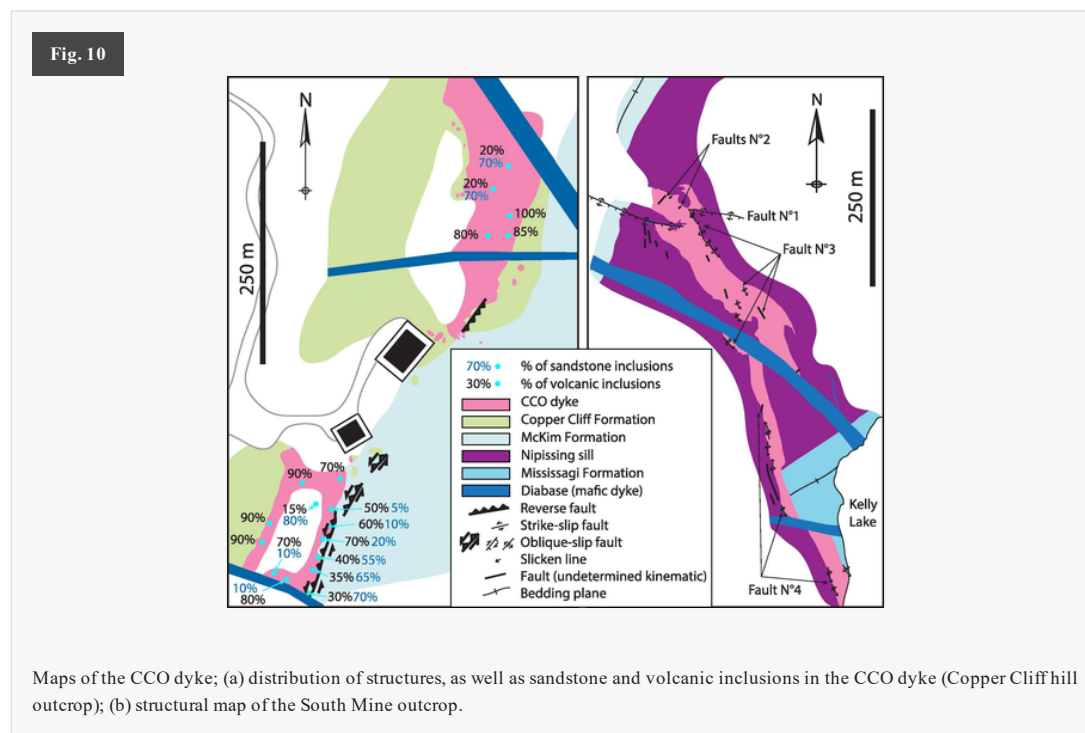
The distribution of inclusion-rich and -poor units is heterogeneous, especially along the eastern margin of the CCE (Fig. 9a). The small inclusion-richest phases concentrate in the core of the CCE (Fig. 9a), while large inclusions and rafts are most abundant along the margins of the CCE (Mathieu et al. 2021¹⁰ [Data in Brief reference to add](#)[Instruction: reference needed (this is the Data-in-brief accompanying publication - I don't know how to cite it)]). The SPO analysis was performed on the small inclusions. Based on these results and the orientation of the contacts between phases with contrasting inclusion contents, trajectories of melt movements were drawn by hand (Fig. 9b). These trajectories correspond to a linear fabric that formed upon solidification of the CCE melt. The trajectories are sub-parallel to the eastern margin of the CCE and trend generally NW–SE in the rest of the embayment. The trajectories locally curve around rafts and spiral in the curved SW-margin of the CCE (Fig. 9b).

4.3 Geology of the CCO dyke

Four outcrops preserved the geological relationships used to understand the emplacement of the CCO dyke. These outcrops are shown in Fig. 2 and detailed field relationships are depicted in Figs. 3, 4, 5 and 9, and Table 3. On the Northern outcrop (Fig. 2), the margin of the dyke is made of QD, which is aphyric and quartz-richer than the inner IQD phase (Fig. 4a; Table 1). Both IQD and QD are equigranular and medium-grained (1 mm) rocks that contain equivalent proportions of mafic (amphibole) and felsic (quartz, feldspar) minerals. Both phases contain 1 to 4 cm long granitoid inclusions and only the IQD phase contains a large amount of 1 cm long inclusions. The IQD - QD contact is sharp and curvi-planar, with no grain size variation observed (melt-melt contact).

On the Copper Cliff outcrop (Fig. 2), the CCO dyke is medium-grained and contains several varieties of IQD and QD, which can be distinguished on the basis of their sulfide- and inclusion-contents (Fig. 4b). The CCO dyke is richer in inclusions and sulfides toward its core and toward its eastern margin in the northern and southern parts of the outcrop, respectively. The margin (and western portion) of the CCO dyke is made of inclusion- and sulfide-poor QD rocks (Fig. 4b). Only the most marginal QD facies are barren of sulfide and can contain up to 40% inclusions, which may have been incorporated from footwall rocks by thermal erosion of the country rocks at the dyke margins (Fig. 6a). At the contact with the SRBB, the CCO dyke is segmented and additional QD varieties (fine-grained light- to darker-colored rocks) are observed (Fig. 5). These color variations suggest incomplete mixing between the CCO and SRBB melts (Fig. 6b), as the Sudbury Breccia matrix was likely a fragment- and melt-body when the CCO dyke formed.

An SPO analysis was conducted on the 1 cm long inclusions exposed in the southern part of the Copper Cliff outcrop and the long over short axes ratio (a/b) varies from <0.7 to >0.9 (Fig. 8f, g). The inclusions are strongly aligned in the N-S to NE-SW directions, parallel to slightly oblique to the eastern margin of the CCO dyke. Also, on the Copper Cliff hill outcrop (Fig. 2), 90% of the inclusions could be identified as sandstone and volcanic rock derived from footwall rocks that are in contact with the CCO dyke; i.e., rocks from the McKim and Copper Cliff formations (Fig. 10a). Sandstone inclusions are most abundant where the dyke is in contact with the McKim Formation, and *vice versa* (Fig. 10a).



On the South Mine outcrop (Fig. 2), the CCO dyke has a fine-grained and dark-colored chilled margin and is mostly made of a medium-grained equigranular rock that contains as much mafic (amphibole, biotite) as felsic (quartz, feldspar) minerals. The QD phase has an irregular contact with the discontinuous IQD inner phase (Fig. 4c). Both the QD and IQD phases contain several 1 to 10 s m long gabbro inclusions with sharp to diffuse contacts, which are derived from the hosting Nipissing sill. Smaller gabbro inclusions are observed within 5 m of the dyke margin, and only the IQD phase contains sulfide and abundant 1 cm long rounded inclusions. This part of the dyke also contains 1 cm long sandstone inclusions, which are likely derived from the McKim Formation located ~200 m to the north of these inclusions.

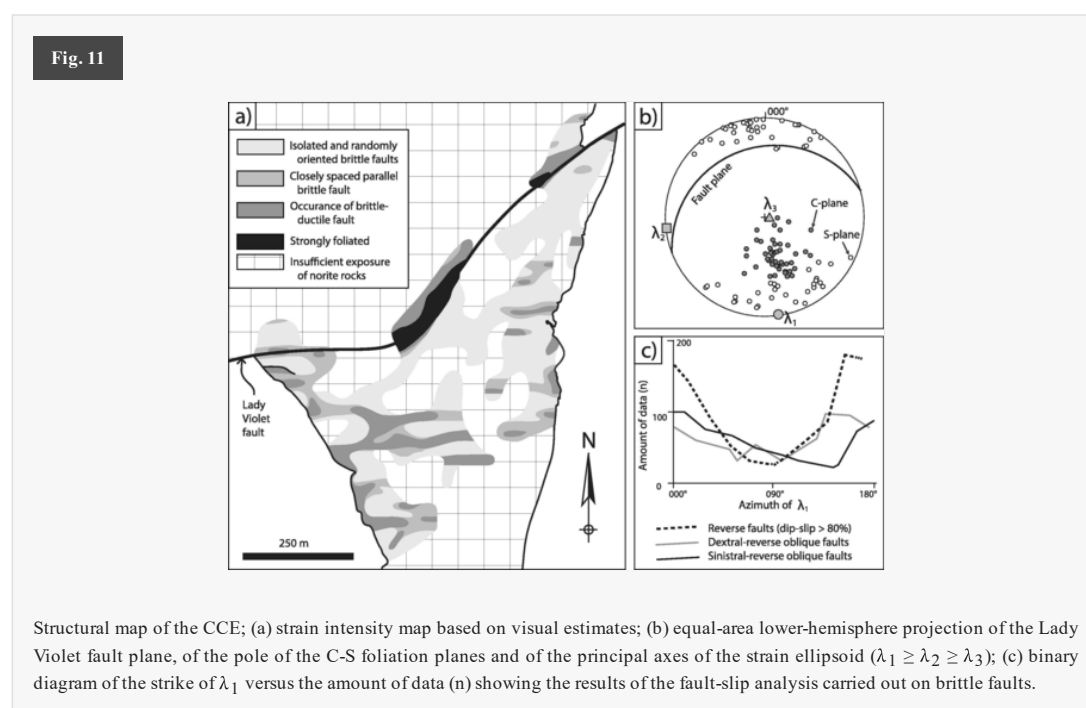
On the southern outcrop (Fig. 2), the CCO dyke is equigranular and mostly medium-grained. A slight grain-size reduction is observed within 1–2 m from the margin of the dyke (chilled margin). The dyke is made of QD that contains rare cm-long sandstone inclusions. The QD phase is made of equal amounts of amphibole and felsic minerals (quartz, feldspar), and local quartz-enrichment is observed. In general, the thickness of the dyke and the IQD/QD ratio decrease southward, while the thickness of the quenched margin increases (Table 3).

4.4 Structural data

The SIC has been folded and faulted by several post-cratering deformation events. In the CCE, this formed brittle-ductile shear zones ($n = 80$ measured) with centimeter-scale slip magnitudes. These structures have reverse to reverse-dominated (60% to >80% of dip-slip component) and oblique-slip kinematics. The fault planes mostly strike 090° and dip steeply, with slicken lines oriented $150/50$ SE. The brittle faults measured in the CCE ($n = 2409$) have ~ 1 cm slips and sometimes contain *syn*-kinematic minerals such as quartz, muscovite, biotite and, more often, chlorite. These structures have mostly reverse or reverse-dominated kinematics. The fault planes mostly strike 070° – 090° and, to a lesser extent, 050° and 130° , and dip 50° to 89° toward the south.

In the CCO dyke, most brittle and brittle-ductile faults are oriented E-W and have accommodated horizontal shortening, e.g., Fault N°1 (Table 5). Some faults also formed along the margin of the dyke (Fig. 10a, b). For example, in the South Mine outcrop (Fig. 10b), faults N°3 and N°4 are oriented $150/90^\circ$, have displaced the gabbro-sandstone contact by 57–105 m, and have displaced fault N°1 by 12 m. The total slip magnitude of these NNW-SSE-striking faults is between 12 and 165 m, and a part of this slip may have been accommodated by a pre-impact fault that was then occupied by the CCO dyke.

The distribution of faults in the CCE was used to produce a strain intensity map (Fig. 11a). Maximum strain intensity is attributed to the Lady Violet fault (described below), and lower strain intensities are attributed, in decreasing order, to areas that contain brittle-ductile faults, swarms of brittle faults and isolated brittle faults. High-strain planar fabrics are oriented E-W in the center of the CCE (Fig. 11a). Strain intensity is also elevated along lithological boundaries that constitute a major break in mechanical competency, such as the western margin of the CCE.



The CCE and CCO dyke are also intersected by several faults with m to km slip magnitudes. In the CCE, the Lady Violet fault is 5 m wide in plan view and C-S fabrics point to reverse sense-of-displacement on a fault oriented $080/30$ – 50 NW ($n = 135$), with slicken lines trending 170° – 000° ; i.e., 20%-10% of sinistral strike-slip motion (Fig. 11b). The Lady Violet fault has displaced the margins of the CCE by 70–90 m in plan view and has an estimated total slip magnitude of 400–520 m. East of the CCE, the fault is <1 m wide NE-SW fault with strike-slip kinematics (Table 5).

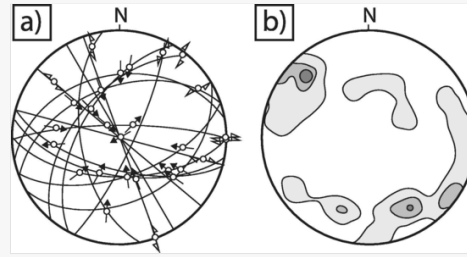
The N°2-X fault is known from Vale underground surveys to be a $040/55$ NW oriented fault with an apparent horizontal dextral motion of 400 m. Using slicken lines measured underground and at surface, on brittle structure parallel to the main fault, the total slip magnitude of the N°2-X fault is estimated at 415–620 m. At surface, the Creighton fault strikes E-W, has a dextral motion and displaces the CCO dyke by 580 m (Cochrane, 1983). Underground, faults parallel to the Creighton fault appear within a distance of 1 km on either side of the main fault plane. Slicken lines measured underground and at surface point to oblique-slip and strike-slip kinematics of the faults, and the total slip magnitude amounts to 580–3300 m (Table 5).

The 830 shear zone is a 160° -striking and west-dipping fault (Mytny, 2006). This fault was observed underground and at surface, in footwall rocks, where it is a 20–100 m wide N-S-striking and sub-vertical fault. The 830 shear zone displaces the contact between the McKim Formation and the Nipissing gabbro, and has a total slip magnitude of about 80 m. The Evan fault has displaced the CCO dyke by 60 m (dextral motion) and has a total dextral oblique-slip magnitude estimated at 175 m. The northern segment of the E-W-striking Murray fault formed 030° -trending slicken lines in the CCO dyke and has an estimated total slip magnitude of 2.7 km (Table 5).

In summary, the major faults that intersect the CCO dyke are oriented E-W and, to a lesser extent, NNW-SSE and NE-SW (Fig. 12a). The orientations of the maximum principal paleostress axes, sigma 1, are estimated for each fault using

the measured slicken lines. Sigma 1 was a sub-horizontal and 130° to 150°-trending vector that was contained in a plane defined by the shear and normal stresses (Fig. 12b).

Fig. 12

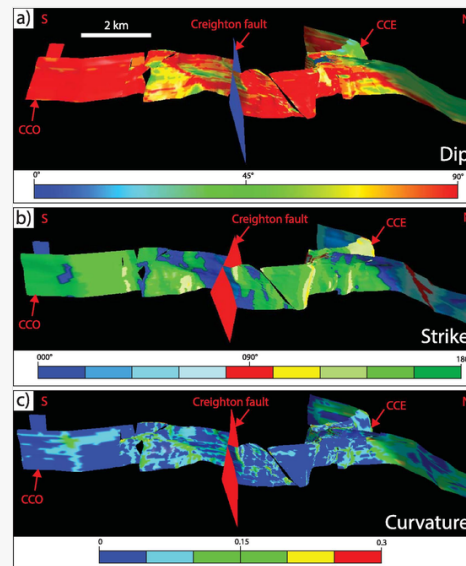


Angelier diagram (a) and contour plot (b) for the major faults that intersect the CCO dyke ($n = 28$ data); (a) averaged orientation of the fault planes and slicken lines; (b) sigma 1 orientations.

4.5 Three-dimensional (3D) modelling

A 3D Move model furnishes information on the general attitude of the CCE and CCO dyke contacts and it provides a basis to restore the CCO dyke and CCE to their pre-deformation geometries. In 3D, the CCE is shown to correspond to an abrupt morphological change in the orientation of the crater floor (Fig. 13a, b). The CCE thins from 1.6 km to 60 m southward and downward, and it is no longer observed beneath the -500 m elevation. The CCE has a funnel shape and dips 30° – 40° toward the NW and NE, and the crater floor dips 50° – 75° NW. The CCO dyke, in turn, is a sub-vertical (mean dip of 85°) intrusion along most of its length, except south of the Creighton fault, where it dips 60° – 70° E (Fig. 13a).

Fig. 13



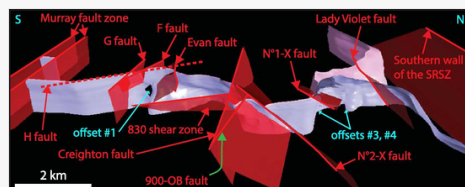
Perspective views of the 3D Move model, with the eastern flank of the CCO dyke and CCE color-coded based on dip (a), strike (b) and curvature (c) data.

The CCO dyke strikes 160° to 180° , except where it connects to the CCE and in the vicinity of the Creighton fault, where it strikes 090° and 010° , respectively (Fig. 13c). The curvature, which describes the amplitude of the variation in orientation of a surface, is equal to zero along most of the length of the dyke, except in a few areas with limited extents (Fig. 13c). This indicates that the CCO dyke is made of several segments with constant orientations that are connected by narrow curved dyke segments. According to observations based on the Datamine 3D model of Vale, the thickness of the CCO dyke varies southward and downward from 50 to 60 m to 10–30 m, although the modelled geometry is

based on drill holes that intersect the dyke at moderate to low angles from surface to depth, respectively, and the thickness estimate is less certain at depth. The CCE corresponds to an abrupt northward and upward thickening of the CCO dyke, from 50 m to 100 s of meters.

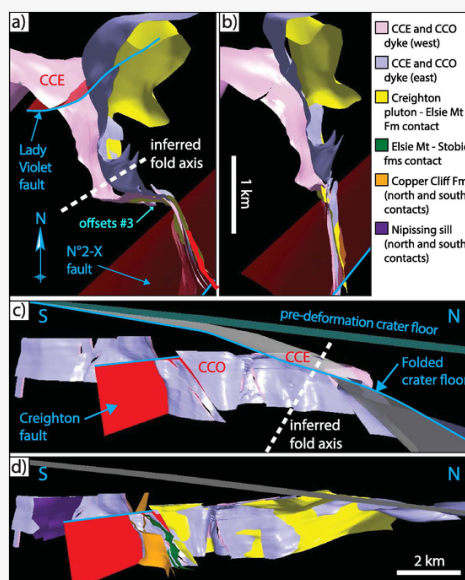
The CCO dyke is segmented by several faults, but also displays offsets (Offset #1, #2, #3 and #4) that are not spatially associated with faults (Fig. 14). Offset #1 is observed south of the Evan fault, from elevation -270 m and deeper. At the -2500 m elevation, the horizontal distance between the dyke segments is 585 m. The CCO dyke is oriented $160/90^\circ$ and $170/65$ E south and north of Offset #1, respectively, and is thicker north of the offset. Offset #2 is only observed on the Datamine 3D model, which goes to lower elevations than the 3D Move model, and is likely the result of ductile deformation along the 830 shear zone. Offset #3 is observed beneath the tip of the CCE, from elevation -190 m and deeper (Fig. 15a). There, the width of the CCO varies from 30 to 60 m to >200 m, SE and NW of the offset, respectively. Offset #4 is located beneath the CCE and the CCO dyke is thicker (200 m) south than north (60 m) of the offset (Fig. 14).

Fig. 14



Perspective view of the 3D Move model displaying the major faults that intersect the CCO dyke.

Fig. 15



Perspective views of the 3D Move model; (a) top view of the model showing an inferred fold axial plane oriented $060/90^\circ$; (b) top view of the un-faulted model un-folded using an inferred fold axis oriented $060/90^\circ$; (c) perspective view of the un-faulted model un-folded using an inferred fold axial plane oriented $060/90^\circ$, and showing an inferred fold axis oriented $045/60$ SE; (d) perspective view of the un-faulted model un-folded using inferred fold axial planes oriented $060/90^\circ$ and $045/60$ SE. Abbreviations stand for Formation (Fm) and formations (fms).

The main lithological contacts observed in footwall rocks were geometrically modelled in 3D. The CCO dyke strikes oblique to these lithological contacts along most of its length, except in its northern tip, where it follows the Creighton pluton to Elsie Mountain Formation contact (Mathieu et al. 2021[Instruction: reference needed (this is the Data-in-brief accompanying publication - I don't know how to cite it)]0--Data in Briefreference to add). Also, in the vicinity of the Creighton fault, the CCO dyke is sub-parallel to the contact between the Mc Kim and Copper Cliff formations.

The 3D Move model was used to estimate the total slip magnitude of the main faults that intersect the CCE and CCO dyke. Post-impact total slip magnitudes were estimated using the fault kinematics deduced from field observations and modelling (Table 2), using the 3D location of the CCO dyke on either sides of the fault planes and confirmed by restoring the Move 3D model to its pre-faulting geometry (Fig. 15). The displacement of some faults decreases rapidly downward (Evan and F faults) or upward ($N^\circ 1-X$ fault), while other faults have accommodated homogeneously distributed total slips. These total slip magnitudes are in agreement with those deduced from field observations, except for the 830 shear zone (Mathieu et al. 20210--Data in Briefreference to add[Instruction: reference needed (this is the

Data-in-brief accompanying publication - I don't know how to cite it)). This fault is a wide ductile shear zone that curved the CCO dyke and that may have accommodated as much as 600 m of sinistral normal oblique-slip displacement. Restoring the area deformed by the 830 shear zone restores the CCO into a straighter and thicker dyke segment. In general, most local variations in orientation observed along the CCO dyke can be attributed to post-cratering fault motion.

Once un-faulted, the 3D Move model was restored to its pre-folding geometry. In the northern part of the study area, the granitoid-basalt contact, the tip of the CCE and the northern part of the CCO dyke are curved in plan view (Fig. 15 a). This geometry may result from folding, i.e., a fold-axial plane oriented 060/90° and sub-vertical fold axis. Axial planar fabrics are not exposed in the field, and the existence of the fold-axial plane oriented 060/90° remains speculative. Restoring the 3D Move model around this postulated fold axis has straightened both the CCE and CCO dyke into N-S trending intrusions and preserves the enlarged geometry of the southern part of the embayment (Fig. 15 b).

The crater floor was then restored to its initial, potentially sub-horizontal (Grieve et al., 2008), position. North of the study area, the crater floor has the shape of a synform (Boerner et al., 1999) and it likely takes the shape of an antiform in the study area (Lenauer and Riller, 2012a, 2017). The crater floor was restored as a sub-horizontal surface dipping 06° toward the NW, using a fold-axial plane oriented 045/60 SE and a sub-horizontal fold axis (Fig. 15c). Un-folding mostly stretches the 3D Move model in the CCE area (Fig. 15d).

5 Discussion

Field data provide important constraints on the formation of the CCE and CCO dyke, as will be discussed first, prior to summarizing the effect of post-cratering deformation on the rocks of the study area.

5.1 Development of the CCE on the crater floor

The CCE is made of two main types of rocks, phases V and II (Fig. 7b), which likely correspond, respectively, to the gabbro-norite and quartz monzogabbro-norite (Capes, 2001). Phase V is sulfide-richer than phase II (Fig. 7c). The other phases I, III, IV and VI have limited volumes and may correspond to phases V and II melts modified by the assimilation of inclusions. Small (<10 cm long) inclusions are most abundant in the core of the CCE, whereas larger inclusions concentrate along the margins (Fig. 9).

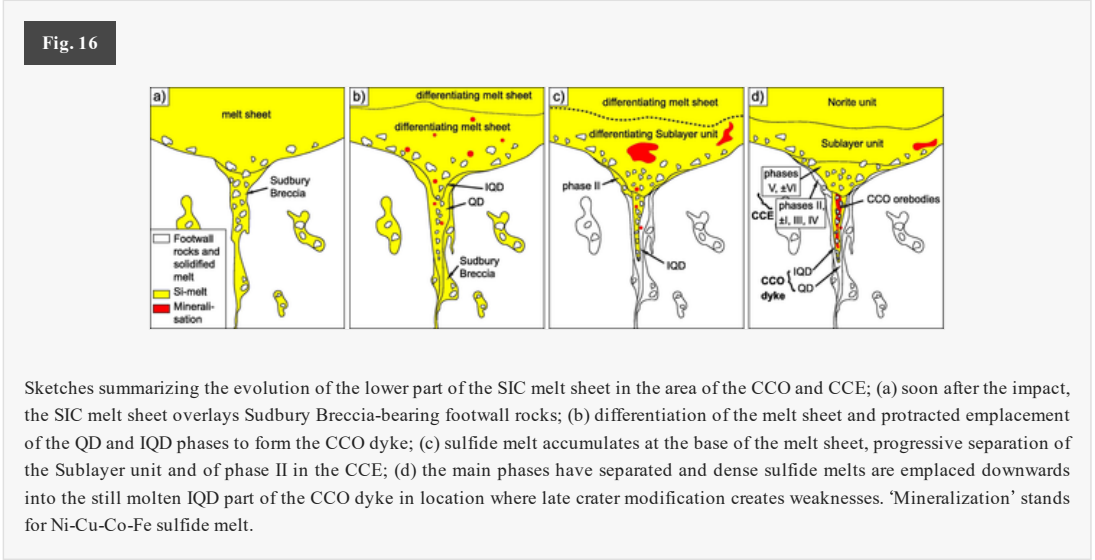
Phase II also has a finer grain size and concentrates in the western part of the CCE, whereas the eastern part of the CCE is made of a thin layer of phase III, a coarse-grained and porphyroblast-barren equivalent of phase II (Fig. 7). Grain-size distribution indicates that the eastern half of the CCE has cooled more slowly than its western half (Fig. 3). A possible explanation is that the CCE was initially made of phase II, which cooled due to its proximity with footwall rocks, and that it was then invaded by a hotter melt (phase V). This occurred while phase II was still molten and explains the abundance of phase II inclusions in phase V (Fig. 7b). This also accounts for the distribution of inclusions, which are larger along the margins than in the core of the CCE, where the melt had more time to thermally erode and break down large inclusions.

The large inclusions in the CCE are mostly granitoid (80%) and volcanic (20%) rocks. These lithologies are abundant along the southern contact of the SIC (Fig. 1) and the inclusions may have been laterally transported over long distances in the melt sheet. However, most inclusions are granitoid rocks, possibly because the CCE has mostly developed in the Creighton pluton or close to its contact with its volcanic host rocks. This indicates that inclusions are locally derived in the CCE. The locally derived large inclusions are most abundant along the margins of the CCE, in phase II. Phase V is enriched in small inclusions with undetermined origins, which may correspond to broken down large inclusions, as postulated above, or point to a more distal origin.

The CCE was thought to have the geometry of a trough (Morrison, 1984) but 3D modelling of the original shape indicates a more irregular and complex shape. It likely formed during crater-floor modification by thermal erosion and slumping processes (Ames et al., 2007; Morrison, 1984). Given the abundance of locally derived inclusions, the CCE may have initiated as an abnormally thick Sudbury Breccia body that formed at the contact between granitoid and volcanic footwall rocks and localized in the most easily fused country rocks, i.e., granitoid. This irregularity may then have enlarged as it was invaded by melt from the base of the SIC, which may have mixed with the Sudbury Breccia melt to form phase II.

Phase V is more mafic than phase II and it contains abundant sulfide mineralization and small inclusions of undetermined origin. Phase V is similar to rocks of the Sublayer unit, which is described as a unit that contains silicate-free massive sulfide bodies (Lightfoot, 2017; Souch et al., 1969) and which represents one of the most mafic parts of the SIC (Grant and Bite, 1984; Hecht et al., 2008; Lightfoot, 2017; Murre, 2000; Prevec and Cawthorn, 2002; Wood and Spray, 1998). After phase II invaded the CCE, the melt sheet may have continued to differentiate. At this stage, sulfide-rich melt concentrated in the lower part of the melt sheet and invaded the CCE, forming phase V that mingled

with phase II (Fig. 16). Melt sheet differentiation may then have continued, progressively forming the Sublayer unit beneath the Main Mass of the SIC (Keays and Lightfoot, 2004).



Two main mechanisms have been proposed to account for the Sublayer: 1) settling of dense materials on the floor of the impact crater (Lightfoot, 2017); and 2) incorporation of mafic pre-impact rocks by the lower part of the layered melt sheet (Lightfoot, 2017; Lightfoot et al., 1997a; Prevec and Cawthorn, 2002; Zieg and Marsh, 2005). In the CCE, phase V contains more small inclusions than phase II, and is unlikely to have evolved toward a more mafic composition by preferentially assimilating mafic volcanic over granitoid inclusions. Settling of dense material on the crater floor is thus more likely. This material may then have been trapped in the CCE below the convecting melt of the main melt sheet.

Melt trajectories deduced from field observations (Fig. 9b) may indicate that the CCE melt flowed downward and/or outward, and toward the CCO dyke. The embayment and the offset dyke have a large contact surface with footwall rocks and likely cooled more rapidly than the rest of the melt sheet, as indicated by the quenched dioritic rocks at the margin. It is also possible that the CCE and CCO dyke formed before melt sheet differentiation (Lightfoot, 2017).

5.2 Formation of the CCO dyke

The CCO is an approximately N-S-striking dyke, the thickness of which decreases southward from 100 to 3 m. The southernmost part of the dyke cooled more rapidly, as indicated by the thicker quenched margins (Grant and Bite, 1984), and the QD/IQD ratio increases southward (Table 4). The IQD-QD contact is a melt-melt contact, indicating a protracted emplacement of QD and IQD phases, as observed in other Offset dykes (Lightfoot, 2017; Pillés et al., 2017).

Table 4

i The table layout displayed in this section is not how it will appear in the final version. The representation below is solely purposed for providing corrections to the table. To preview the actual presentation of the table, please view the Proof.

Geological characteristics of the CCO dyke.

Outcrops	Thickness of the CCO (m)	CCO content in		Chilled margin thickness (m)
		IQD	QD	
North Mine	100 to 85	~60%	~40%	0.01 to 0.02
Copper Cliff hill	85	64%	36%	(0 to 2)
South Mine	45 to 13	34%	66%	0.1 to 0.5
Southern outcrop	20 to 3	0%	100%	1 to 2

Table 5

i The table layout displayed in this section is not how it will appear in the final version. The representation below is solely purposed for providing corrections to the table. To preview the actual presentation of the table, please view the Proof.

Averaged orientation of the main faults.

Fault	Fault planes	Kinematics	Dip-slip	Total slip
-------	--------------	------------	----------	------------

Fault N°1	090/60 S	Dextral-normal oblique-slip	45%	28.4 m
Fault N°3 and 4	150/90°	Sinistral strike-slip, oblique-slip	25% to 60%	12–165 m
Lady Violet fault (in CCE)	080/30–50 NW	Sinistral reverse oblique-slip	80%	400–520 m
Lady Violet fault (east of CCE)	050/90°	Sinistral strike-slip	20% to 40%	
N°2-X fault	040/55 NW	Dextral reverse oblique-slip	50% to 80%	620–415 m
Creighton fault	090/80 N	dextral Strike-slip, oblique-slip	15% to 85%	580–3300 m
830 shear zone	010/80 NW	Sinistral and oblique-slip	80%	80 m
Evan fault	060/40 SE	Dextral reverse oblique-slip	85%	175 m
Murray fault	100/60 SW	Dextral reverse oblique-slip	50% to 80%	2.7 km

The CCO dyke is concordant to, and intruded into, bedding, foliation and fault planes. It is not unusual for sheet intrusions to propagate concordant to pre-existing planar discontinuities (Mathieu et al., 2008; Mathieu and van Wyk de Vries, 2009). Following cratering, target rocks at discontinuities may have preferentially been affected by shock melting and fragmentation, forming a network of Sudbury Breccia bodies that may have been exploited by CCO melt. A heterogeneous spatial distribution of the Sudbury Breccia bodies in footwall rocks may also explain Offsets #1, #3 and #4 observed along the CCO dyke, e.g., the offset spatially associated with the SRBB that is observed on Copper Cliff hill outcrop (Fig. 4b). Also on the Copper Cliff hill outcrop, the QD melt mingled and possibly mixed with SRBB melt, demonstrating that the Sudbury Breccia bodies were still mobile when the CCO dyke formed. This is consistent with chemical investigations carried on Offset dykes and embayments that point to limited local assimilation of footwall rocks (Capes, 2001; Lightfoot et al., 1997b). The SRBB melt was likely cooler and more viscous than QD when the CCO dyke formed, and viscosity contrast between QD and SRBB melts limited mixing.

Mingling between CCO dyke and Sudbury Breccia melts is also consistent with most existing hypotheses, which suggest that the Offset dykes formed after cratering, during long-term crater modification (Hecht et al., 2008; Hubert et al., 2020; Murre, 2000; Riller, 2005; Wichman and Schultz, 1993). The Offset dykes may have been filled first with undifferentiated melt representative of the original bulk composition of the melt sheet (Lightfoot, 2017; Lightfoot et al., 1997b; Scott and Benn, 2002). The Hess dyke, however, is made of a melt evolved from the norite unit, which points to protracted Offset dyke formation (Wood and Spray, 1998). Offset dykes also have more felsic compositions than typical Sublayer rocks (Lightfoot et al., 1997a), suggesting that they formed prior to complete melt sheet differentiation. We propose that the CCO dyke formed after cratering, while the SIC had started to differentiate and the Sublayer had not fully evolved into a mafic and sulfide-rich unit, possibly on time scales of tens to hundreds of thousand years after impact.

Discontinuities possibly filled with locally molten (Figs. 4b and 6) Sudbury Breccia melt provided an easy pathway for the SIC melt, which may then have injected downward. This hypothesis is more consistent with a passive downward injection of the melt (Hecht et al., 2008; Murre, 2000) than with a forceful injection (Grant and Bite, 1984; Pattison, 1979; Prevec and Büttner, 2018). The CCO dyke has a uniform N-S-strike, suggesting that it may have followed a structure, locally filled with solidified and/or mobile Sudbury Breccia melt (see below), that accommodated long-term crater modification (Hecht et al., 2008; Murre, 2000; Riller, 2005; Wichman and Schultz, 1993). In the field, the CCO dyke injects small fingers into foliation planes and brecciated footwall rocks (Southern Mine outcrop), which may correspond to dilation zones infiltrated by melt. The CCO dyke may have injected in mechanically weakened rocks and within a deformation regime that promoted local dilation during long-term crater modification.

Both QD and IQD phases contain inclusions. The sandstone inclusions observed on the South Mine outcrop, where the dyke is in contact with gabbro, and the results of SPO analyses, point to some lateral transport. However, lateral transport of inclusions is limited in the CCO dyke as most inclusions are locally derived. Given the sub-vertical orientation of bedding in footwall rocks, inclusions would seem locally derived even if they had been transported in a direction orthogonal to the erosion surface, and such transport cannot be excluded. However, these locally derived inclusions ruled out a derivation from an evolved Sublayer unit more or less homogenized by convection movements, and the CCO dyke likely formed prior to Sublayer separation from the Main Mass. We propose that inclusions were detached from footwall rocks during impact and cratering, as Sudbury Breccia melt was forming. The CCO melt later invaded the area occupied by Sudbury Breccia melt and inclusions, inducing limited lateral and vertical transport of inclusions, as well as decoupling between melt and inclusions movement.

Also, the quartz, feldspar and mafic minerals proportions are relatively constant over the whole length of the CCO dyke, despite the abundance of inclusions with different compositions on the four outcrops studied in detail. This indicates that the dyke solidified before any significant assimilation of inclusions by the CCO melt could occur. Field observation of mineral assemblages also suggest chemical similarities between QD and IQD melt, which is also

observed in other Offset dykes (Pilles et al., 2018). This also points to limited assimilation of inclusions and limited mixing between QD and Sudbury Breccia melts.

Offset dykes are commonly interpreted as multiple intrusive events, with QD injecting prior to IQD (Hecht et al., 2008; Lightfoot, 2017; Lightfoot and Farrow, 2002; Murphy and Spray, 2002; Prevec and Büttner, 2018). Alternative hypotheses argue for a continuous injection event and suggest that flow differentiation focused the inclusions, and possibly also the sulfides, in the core of the dyke (Pilles et al., 2018; Prevec and Cawthorn, 2002; Rousell and Brown, 2009). A continuous injection event could explain the chemical similarities between QD and IQD melt (Pilles et al., 2018), but the CCO dyke may not be long enough for flow differentiation processes of the types found in crustal scale dykes (Richardson, 1979) to operate efficiently. In addition, there is a major chemical difference between QD and IQD melt, i.e., QD is S-undersaturated to \pm S-saturated, as confirmed by the few disseminated sulfides observed in QD rocks, while IQD is a S-saturated melt (Lightfoot, 2017), as confirmed by the abundance of disseminated sulfides observed in IQD rocks. Also, size distribution of inclusions is random in the IQD phase, while a symmetric distribution of inclusion sizes within the CCO dyke would be expected if the flow differentiation process was operating. The sharp contact between QD and IQD observed in the outcrops described here results from the protracted emplacement of melts with contrasting chemistry (S-saturation differences) and inclusion contents (Lightfoot, 2017). A component of late differential movements between the inclusion-laden and inclusion-poor phases (Pilles et al., 2018) is also possible, but flow differentiation is unlikely to be the dominant process responsible for the observed distribution of inclusions.

Thus and like the CCE, the CCO dyke may have formed progressively (Lightfoot and Farrow, 2002), in two main stages: 1) injection of QD melt; 2) solidification of the thinnest, most distal, parts of the dyke; and 3) injection of IQD melt in the still mobile QD parts of the dyke (Fig. 16). We propose that the CCO dyke formed by the downward injection of an undifferentiated SIC melt, which contained a limited amount of inclusions, into a series of brecciated discontinuities, i.e., Sudbury Breccia melt laden with locally derived inclusions. Incremental dilation favors QD injection from a S-undersaturated melt sheet followed by IQD injection from the lower part of the melt sheet after it reached S-saturation. The QD margin of the dyke was in contact with footwall rocks for a longer time span and was likely cooler and more viscous than the IQD phase; viscosity contrast between QD and IQD prevented mixing of the QD and IQD phases, which explains the sharp contacts observed in the field. The IQD phase is locally observed along the eastern margin of the CCO dyke, possibly because IQD generally infiltrated the molten QD core of the dyke and may have locally infiltrated planar discontinuities such as the contact between footwall rocks and the solidified QD margin of the dyke. QD may then have solidified before IQD. Continuous differentiation of the melt sheet induced separation between the Sublayer and Main Mass, and sulfide melts accumulated as irregularly distributed bodies in the Sublayer unit (Keays and Lightfoot, 2004). These dense sulfide melts may then have dripped in the still-molten parts of the CCO dyke, i.e., mostly IQD at this stage, explaining the spatial association between IQD and mineralization (Fig. 16). This hypothesis suggests a protracted dyke formation and decoupling between silicate magma and sulfide melt, which is not uncommon in other magmatic systems (Leshner, 2017).

5.3 Post-SIC deformation

Several post-impact shortening events have folded and faulted the SIC and footwall rocks (Clendenen et al., 1988; Cowan and Schwerdtner, 1994; Dreuse et al., 2010; Milkereit and Green, 1992) and each event is associated with NW-SE shortening (Bailey et al., 2004; Papapavlou et al., 2018; Tschirhart and Morris, 2012). Evaluating the influence that regional NW-SE shortening had on the geometry of the SIC is important in the discussion of the validity of the hypotheses formulated in the previous sections, but also has implications for mineral exploration. In the study area, major faults are best exposed in footwall rocks, where they have recorded pre- and post-impact deformation events. However, faults with long slip histories tend to retain the markers of their latest motion. The bulk of kinematic markers measured in the field likely portrays post-impact movement as the markers measured on the major faults in footwall and SIC rocks, as well as those of the small brittle faults measured in SIC rocks, are similar.

NW-SE shortening is expected to form faults chiefly parallel to the NE-SW-striking SRSZ thrust fault system in SIC rocks (Fig. 1). However, the study area is located in the South Range, which consists of two tectonically different portions (Santimano and Riller, 2012): 1) the western South Range that formed by thrusting on the SRSZ; and 2) the eastern South Range that underwent dextral transpression (Cowan et al., 1999; Santimano and Riller, 2012) generating the southeastern lobe of the SIC by buckling (Cowan and Schwerdtner, 1994). The study area is located at the western portion of the eastern South Range where, according to lineaments mapped from air photos, NNW-SSE and NE-SW striking sinistral conjugate faults and NW-SE striking dextral faults are consistent with N-S shortening (Lenauer and Riller, 2012a; Santimano and Riller, 2012).

In the CCE, deformation was mostly accommodated by sub-vertical and E-W-striking faults, and faults and quartz veins have consistent orientations and kinematics, i.e., oblique-slips and reverse-dominated kinematics. Local N-S shortening (Lenauer and Riller, 2012a; Santimano and Riller, 2012) is expected to induce dip-slip dominated reverse motion along E-W-striking planar structures. It is possible that pre-impact E-W striking faults propagated from footwall rocks and into SIC rocks during regional NW-SE shortening (Lenauer and Riller, 2012a), forming oblique-slip E-W striking faults in the CCE. To test this hypothesis, the orientation of the principal paleo-strain axes is solved using a

fault-slip analysis on the brittle faults for which slicken lines were measured ($n = 1992$). This calculation assumes that these faults formed toward the end of the SIC folding, have accommodated a limited amount of slip and have not been rotated. The fault slip analysis indicates that the maximum principal shortening (λ_1) mostly trends 160° – 020° and is sub-horizontal (0 – 20° dip; Fig. 11c), while the minimum strain axis (λ_3) is sub-vertical. This is consistent with results of fault-slip analysis from the South Range and other portions of the SIC (Lenauer and Riller, 2012a; Riller et al., 2017) and N-S shortening toward the end of the SIC folding (Santimano and Riller, 2012).

In detail, the faults measured in the CCE can be distributed between 070° and 110° -striking reverse faults (35% of the structures), 090 – 130° -striking dextral-reverse oblique faults (34%) and 050 – 100° -striking sinistral-reverse oblique faults (17%), which are associated with λ_1 that trend, respectively, 140 – 030° , 140 – 180° and 170 – 030° (Fig. 11c). Strain partitioning (Lister and Williams, 1983) may have formed the E-W-striking reverse faults (N-S-trending λ_1), which have accommodated a part of the simple shear strain accommodated elsewhere by oblique-slip faults. Additional structures (14%) are NE-SW- and NW-SE-striking conjugate faults along the margin of the CCE, associated with 040° – 110° -trending λ_1 values. The CCE and footwall rocks contain several lithologies, with variably oriented foliation and bedding planes (footwall rocks) and melt-melt contacts (CCE rocks), which may have induced mechanical anomalies that influenced local principal strain direction (Lenauer and Riller, 2012b; Riller et al., 2017), forming NE-SW- and NW-SE-striking conjugate faults.

In the CCE, NW-SE and NE-SW λ_1 trends may reflect variations in the relative magnitude of the main horizontal principal stresses of the local stress field, possibly caused by variations in the magnitude of the remote stress field (Wilkerson et al., 1991). As the magnitude of the remote σ_1 increases and decreases, the local σ_1 becomes parallel, respectively, to the σ_1 and σ_2 of the remote stress field. This hypothesis accounts for the calculated NE- and NW-trending λ_1 and points to similar σ_1 and σ_2 magnitudes. The strain ellipse geometry varies along the SRSZ (Santimano and Riller, 2012; Shanks and Schwerdtner, 1991b) and measurements performed in the CCE are consistent with a prolate strain ellipsoid similar to the ellipsoid shapes deduced in parts of the SRSZ (Shanks, 1991). The shape of these ellipsoids may be a consequence of the confining of the central part of the South Range (Fig. 1) between the extremities of the SIC syncline toward the end of the folding event (Santimano and Riller, 2012).

In the vicinity of the CCO dyke, the major faults are mostly E-W-striking dextral-reverse oblique slip faults and some faults strike NNW-SSE and NE-SW (Fig. 1). These structures display a variety of kinematic markers, indicating strain partitioning along the fault planes and making total slip estimates uncertain. The major E-W-striking faults such as the Murray and Creighton faults pre-date the impact (Cochrane, 1984; Long, 2004; Zolnai et al., 1984) and were likely re-activated by post-impact deformation. The NNW-striking faults could also be pre-impact faults re-activated by long-term crater modification and infiltrated by the CCO dyke (South Mine outcrop; Fig. 2). Other structures, such as the NNW-striking 830 shear zone, have accommodated early ductile deformation of SIC rocks. These faults are sub-parallel to regional shortening and have likely accommodated a limited amount of post-impact sinistral and dip-slip motions. Those correspond to the NNW-striking sinistral structures mapped from air photos in the study area (Santimano and Riller, 2012). Further north, the major NNE-striking sinistral Whitewater Lake Fault Zone also has a sinistral component of movement (Lenauer and Riller, 2012b; Santimano and Riller, 2012).

The NE-SW-striking structures have accommodated dextral to locally sinistral, reverse to locally normal, oblique-slip movements. These structures are sub-parallel to the bedding planes of footwall rocks and orthogonal to the regional NW-SE shortening and should have accommodated the most part of the NW-SE shortening. The E-W-striking faults have however accommodated more total slips than the NE-SW-structures, possibly because footwall rocks contained several E-W faults prior to the impact, and re-activation of these structures has controlled deformation in the study area. Late local N-S shortening interpreted for the study area (Santimano and Riller, 2012) may also have favored E-W-striking faults.

The fault-slip analysis carried out on the major faults indicates that the σ_1 and σ_3 were oriented, respectively, $000/06$ N and $000/84$ S. The slicken lines have variable orientations and are, on average, sub-parallel to regional shortening (Fig. 12). Because the major faults were re-activated, their slicken lines are not oriented 30° from the regional shortening direction. The measured slicken lines are thus markers of the transport direction along the fault planes and not of the orientation of the post-impact stress field.

In summary, footwall rocks contained several E-W- and NNW-SSE-striking pre-impact faults. These structures were re-activated as oblique-slip faults and propagated in SIC rocks to accommodate post-impact deformations. The deformation style observed in the study area contrasts with this observed in the Main Mass of the SIC, where NW-SE-shortening formed NE-SW-striking thrust faults that were then folded into E-W- and NE-SW-striking structures as folding of the SIC progressed (Clark and Riller, 2017). In the study area, pre-impact faults and neo-formed faults accommodated NW-SE shortening, but most kinematic markers registered local N-S shortening associated with late buckle folding of the eastern lobe of the SIC (Cowan and Schwerdtner, 1994; Santimano and Riller, 2012).

5.4 Kinematic restoration of the CCO dyke and CCE in a regional context

Previous kinematic restorations performed on the SIC demonstrated the importance of flexural slip over simple shear, highlighting the importance of the SRSZ in folding the SIC (Clark and Riller, 2018, 2017; Riller et al., 2010a). Such studies also helped locating the pre-folding thickened parts of the SIC, which are spatially associated with known Ni-Cu-PGE mineralization (Clark and Riller, 2018; Dreuse et al., 2010; Lightfoot, 2017). This is consistent with the reconstruction of the general impact crater morphology, which locates the CCE and the southern tip of the CCO dyke beneath, respectively, a thick inner part and a thinner outer part of the melt sheet (Lightfoot, 2017; Ripley et al., 2015).

Using the averaged fault plane orientation and general kinematics deduced from field measurements, the 3D Move model was un-faulted and was then un-folded using various constraints (see Results section; Fig. 15). All of these operations have stretched, straightened and thinned (or locally thickened) the modelled surface of the CCE and CCO dyke. These surfaces have likely been stretched to an un-realistic extent, as the Move software neither takes the slip accommodated by minor structures nor the competency contrasts between weak foliated thin-grained footwall rocks and stiff crystalline SIC rocks into account.

Restoration, however, shows that the CCO dyke has only been slightly tilted by post-impact deformation, i.e., the paleo-vertical is close to today's vertical direction. The sub-vertical pipe-like geometry of the orebodies (Gordon and McDonald, 2015) is thus a pre-deformation feature, which makes the late emplacement model described previously likely. These ore bodies (Gordon and McDonald, 2015) are only observed where the thickness of the dyke is between 30 m and 50 m. According to field data, the <30 m thick parts of the CCO dyke are only made of QD rocks, while >30 m thick portions also contain IQD rocks, confirming the spatial association between orebodies and the IQD phase in the whole CCO dyke. These conclusions are consistent with the CCO dyke formation model proposed in the previous sections.

6 Conclusions

The SIC is a unique melt system, as it corresponds to a large-volume impact melt sheet that formed almost instantaneously in the upper crust (Hubert et al., 2020). Field investigations and structural restoration carried for the need of this study are consistent with protracted formation of the CCO dyke by passive downward melt flow into fractured footwall rocks weakened by Sudbury Breccia inclusion-rich melt bodies. By contrast, in other contexts, dykes are more often injected upward or laterally and generally force their ways through country rocks (Mathieu et al., 2008).

The CCO dyke likely formed during long-term crater modification, while the Main Mass of the SIC was a melt, and its emplacement bracketed a period of time in which the melt sheet changed from sulfide undersaturated to sulfide saturated. The first phase of sulfide undersaturated QD formed the CCO dyke, and this was followed by the injection of sulfide-saturated melt (IQD) once sulfides started to collect toward the base of the melt sheet. The inclusions are locally derived and may have been incorporated by QD and mostly IQD melts, as they flowed downward to form the CCO dyke. The CCE likely enlarged progressively and mostly evolved after the CCO dyke was emplaced. The accumulation and downward emplacement of sulfide melts may have occurred last to form the ore bodies. As the thinner and QD-dominated lower part of the CCO dyke had already solidified, sulfide melts found no weaknesses along which they could migrate downward and remained in the IQD phase of the dyke.

This study indicates a physical decoupling between inclusions, silicate-rich and sulfide-dominated melts, which were emplaced in a semi-continuous process, but comprise three fundamentally distinct events with respect to the sulfide saturation history of the overlying melt sheet and the instability of the crater floor. Another finding, which will need to be validated by chemical investigations, is that the melts of the CCE and CCO dyke may have mixed with Sudbury Breccia melt and that there is no evidence of significant assimilation of the numerous inclusions observed in the field. This suggests that the melt became rapidly unable to assimilate footwall rocks.

The 3D Move model was used to determine total slip magnitudes on the major faults that intersect the CCO dyke, which is important data for exploration. Restoring the model to its pre-deformational shape explains most strike and dip variations observed along the CCO dyke and confirms that the dyke was not significantly rotated, which is consistent with the protracted downward migration of QD, IQD and dense sulfide melts into the evolving dyke.

7 Data availability

Maps, photographs, structural data measured in the field and perspective views of the Move 3D model are available in a co-submission to *Data in Brief* (Mathieu et al. 2020) [Instruction: reference needed (this is the Data-in-brief accompanying publication - I don't know how to cite it)] ~~--Data in Brief reference to add).~~

Declaration of Competing Interest

The authors declare that they have no known competing financial interests or personal relationships that could have appeared to influence the work reported in this paper.

Acknowledgments


Thanks are addressed to **editor-in-chief Huayong Chen**, associate editor Deru Xu, **to reviewer James Darling**, and to **a two-a** anonymous reviewers. Thanks are also addressed to the geologists of the Copper Cliff Mine and to McMaster University field assistants, namely Gordon Bailey, James McDonald, Joseph d'Olivera, Kristen Simpson and Peter Stewart. The study as was carried in collaboration with and supported by Vale, Copper Cliff, as well as the Center of Excellence for Mining Innovation, Sudbury, under RA 1353-CA-030. U.R. acknowledges support from the German Research Foundation (Ri 916/14-1) and L.M. acknowledges support from NSERC (Natural Sciences and Engineering Research Council) Discovery grant (reference number RGPIN-2018-06325) and from the Metal Earth project (Canadian first research excellence fund).

Appendix A Supplementary data

Supplementary data to this article can be found online at <https://doi.org/10.1016/j.oregeorev.2021.104071>.

Reference Instruction: Please add the following references to the list:
Corfu, F., Lightfoot, P.C., 1996. U-Pb geochronology of the sublaver environment, Sudbury Igneous Complex, Ontario. Econ. Geol. 91, 1263–1269.

Davis, D.W., 2008. Sub-million-year age resolution of Precambrian igneous events by thermal extraction-thermal ionization mass spectrometer Pb dating of zircon: Application to crystallization of the Sudbury impact melt sheet. Geology 36, 383–386.

 The corrections made in this section will be reviewed and approved by a journal production editor. The newly added/removed references and its citations will be reordered and rearranged by the production team.

Ames, D.E., Davidson, A., Buckle, J.L., Card, K.D., 2005. Geology, Sudbury bedrock compilation, Ontario. Geol. Surv. Canada, Open File 4570

Ames, D.E., Farrow, C.E.G., Goodfellow, W.D., 2007. Metallogeny of the Sudbury mining camp, Ontario. Miner. Depos. Canada A Synth. major Depos. Dist. Metallog. Evol. Geol. Prov. Explor. methods Geol. Assoc. Canada. Miner. Depos. Div. Spec. Publ. 5, 329–350.

Bailey, J., Lafrance, B., McDonald, A.M., Fedorowich, J.S., Kamo, S., Archibald, D.A., 2004. Mazatzal Labradorian-age (1.7 1.6 Ga) ductile deformation of the South Range Sudbury impact structure at the Thayer Lindsley mine, Ontario. Can. J. Earth Sci. 41, 1491–1505.

Bethune, K.M., 1997. The Sudbury dyke swarm and its bearing on the tectonic development of the Grenville Front, Ontario, Canada. Precambrian Res. 85, 117–146.

Bleeker, W., Kamo, S., Ames, D., 2013. New field observations and U-Pb age data for footwall (target) rocks at sudbury: towards a detailed cross-section through the sudbury structure (extended abstract). In: Large Meteorite Impacts and Planetary Evolution V Meeting. Lunar and Planetary Institute, Houston, Texas, p. 13.

Boerner, D.E., Milkereit, B., Dressler, B.O., Sharpton, V.L., 1999. Structural evolution of the Sudbury impact structure in the light of seismic reflection data. Impact cratering Planet. Evol. II, Boulder Color. Ed. by B. Dressler, VL Sharpton. Geol. Soc. Am. Spec. Pap. 339, 419–430.

Buchan, K.L., Card, K.D., Chandler, F.W., 1989. Multiple ages of Nipissing Diabase intrusion: paleomagnetic evidence from the Englehart area, Ontario. Can. J. Earth Sci. 26, 427–445.

Capes, P.C., 2001. A petrological investigation of the Copper Cliff embayment structure, Sudbury, Ontario Unpublished Master thesis University of Toronto, Ontario.

Card, K.D., 1978. Geology of the Sudbury-Manitoulin Area: Districts of Sudbury and Manitoulin. Ontario Ministry of Natural Resources:[Map Unit, Public Service Centre.

Clark, M.D., Riller, U., 2018. 3-D kinematic restoration of the eastern Sudbury Igneous Complex, Canada, and its importance for Cu-Ni-PGE sulphide exploration. Ore Geol. Rev. 101, 199–210.

Clark, M.D., Riller, U., 2017. Significance of first-order faults in folding mechanically isotropic layers: Evidence from the Sudbury Basin, Canada. J. Struct. Geol. 95, 113–126.

Clendenen, W.S., Kligfield, R., Hirt, A.M., Lowrie, W., 1988. Strain studies of cleavage development in the Chelmsford Formation, Sudbury Basin, Ontario. Tectonophysics 145, 191–211.

Cochrane, L.B., 1984. Ore deposits of the Copper Cliff offset. *Geol. Ore Depos. Sudbury Struct. Ontario Geol. Surv.* 347–360.

Cochrane, L.B., 1983. The Creighton fault: location description, calculation of movement, regional setting and possible mechanisms of formation. Report prepared for Science North

Coleman, A.P., 1902. The Sudbury nickel deposits, Ontario. *Bur. Mines Rep.* 253–303.

Collins, W.H., 1937. The life history of the Sudbury nickel irruptive: IV. Mineralization. *Royal Society of Canada*

Corfu, F., Andrews, A.J., 1986. A U-Pb age for mineralized Nipissing diabase, Gowganda, Ontario. *Can. J. Earth Sci.* 23, 107–109.

Cowan, E.J., Riller, U., Schwerdtner, W.M., 1999. Emplacement geometry of the Sudbury Igneous Complex: structural examination of a proposed impact melt-sheet. *Spec. Pap. Soc. Am.* 399–418.

Cowan, E.J., Schwerdtner, W.M., 1994. Fold origin of the Sudbury Basin, in: *Proceedings of the Sudbury-Noril'sk Symposium*. Edited by PC Lightfoot and AJ Naldrett. *Ontario Geological Survey, Special.* pp. 45–55.

Dressler, B.O., 1984. The effects of the Sudbury event and the intrusion of the Sudbury Igneous Complex on the footwall rocks of the Sudbury Structure, in: *The Geology and Ore Deposits of the Sudbury Structure*. *Ontario Geological Survey Ontario*, pp. 97–136.

Dreuse, R., Doman, D., Santimano, T., Riller, U., 2010. Crater floor topography and impact melt sheet geometry of the Sudbury impact structure, Canada. *Terra* 463–469.

Fahrig, W.F., West, T.D., Hearty, D.B., 1986. Diabase dyke swarms of the Canadian Shield. *Geological Survey of Canada*

Fleet, M.E., Barnett, R.L., Morris, W.A., 1987. Prograde metamorphism of the Sudbury igneous complex. *Can. Mineral.* 25, 499–514.

Gordon, S.C., McDonald, A.M., 2015. A study of the composition, distribution, and genesis of pyrrhotite in the copper cliff offset, sudbury, Ontario, Canada. *Can. Mineral.* 53, 859–878.

Grant, R.W., Bite, A., 1984. Sudbury quartz diorite offset dikes: Ontario geological survey special. In: Naldrett, E.G., Giblin, P.E. (Eds.), *The Geology and Ore Deposits of the Sudbury Structure*. *Ontario Geological Survey, Toronto*, pp. 275–300.

Grieve, R.A.F., Morgan, J.V., Artemieva, N., 2010. The evolution of the Onaping Formation at the Sudbury impact structure. *Meteorit. Planet. Sci.* 45, 759–782.

Grieve, R.A.F., Reimold, W.U., Morgan, J., Riller, U., Pilkington, M., 2008. Observations and interpretations at Vredefort, Sudbury, and Chicxulub: towards an empirical model of terrestrial impact basin formation. *Meteorit. Planet. Sci.* 43, 855–882.

Grieve, R.A.F., Stoeffler, D., Deutsch, A., 1991. The Sudbury structure: controversial or misunderstood? *J. Geophys. Res. Planets* 96, 22753–22764.

Hecht, L., Wittek, A., Riller, U., Mohr, T., Schmitt, R.T., Grieve, R.A.F., 2008. Differentiation and emplacement of the Worthington Offset Dike of the Sudbury impact structure, Ontario. *Meteorit. Planet. Sci.* 43, 1659–1679.

Hubert, M., Kovaleva, E., Riller, U., 2020. Modeling the geochemical evolution of impact melts in terrestrial impact basins: Vredefort Granophyre dikes and Sudbury Offset Dikes. *Meteorit. Planet. Sci.* in press

Keays, R.R., Lightfoot, P.C., 2004. Formation of Ni-Cu-platinum group element sulfide mineralization in the Sudbury impact melt sheet. *Mineral. Petrol.* 82, 217–258.

Krogh, T.E., Davis, D.W., Corfu, F., Pye, E.G., 1984. Precise U-Pb zircon and baddeleyite ages for the Sudbury area, in: *The Geology and Ore Deposits of the Sudbury Structure*. *Ontario Geological Survey Toronto, Ont., Canada*, pp. 431–446.

Latypov, R., Chistyakova, S., Grieve, R., Huhma, H., 2019. Evidence for igneous differentiation in Sudbury Igneous Complex and impact-driven evolution of terrestrial planet proto-crusts. *Nat. Commun.* 10, 508.

Launeau, P., Robin, P.-Y., 1996. Fabric analysis using the intercept method. *Tectonophysics* 267, 91–119.

Lenauer, I., Riller, U., 2017. A trishear model for the deformation of the Sudbury Igneous Complex, Canada. *J. Struct. Geol.* 97, 212–224.

Lenauer, I., Riller, U., 2012a. Geometric consequences of ductile fabric development from brittle shear faults in mafic melt sheets: evidence from the Sudbury Igneous Complex, Canada. *J. Struct. Geol.* 35, 40–50.

Lenauer, I., Riller, U., 2012b. Strain fabric evolution within and near deformed igneous sheets: The Sudbury Igneous Complex, Canada. *Tectonophysics* 558, 45–57.

Leshner, C.M., 2017. Roles of xenomelts, xenoliths, xenocrysts, xenovolatilites, residues, and skarns in the genesis, transport, and localization of magmatic Fe-Ni-Cu-PGE sulfides and chromite. *Ore Geol. Rev.* 90, 465–484.

Lightfoot, P.C., 2017. Nickel sulfide ores and impact melts: Origin of the Sudbury Igneous Complex. Elsevier

Lightfoot, P.C., Farrow, C.E.G., 2002. Geology, geochemistry, and mineralogy of the Worthington offset dike: a genetic model for offset dike mineralization in the Sudbury Igneous Complex. *Econ. Geol.* 97, 1419–1446.

Lightfoot, P.C., Keays, R.R., Morrison, G.G., Bite, A., Farrell, K.P., 1997a. Geologic and geochemical relationships between the contact sublayer, inclusions, and the main mass of the Sudbury Igneous Complex; a case study of the Whistle Mine Embayment. *Econ. Geol.* 92, 647–673.

Lightfoot, P.C., Keays, R.R., Morrison, G.G., Bite, A., Farrell, K.P., 1997b. Geochemical relationships in the Sudbury igneous complex; origin of the main mass and offset dikes. *Econ. Geol.* 92, 289–307.

Lister, G.S., Williams, P.F., 1983. The partitioning of deformation in flowing rock masses. *Tectonophysics* 92, 1–33.

Long, D.G.F., 2004. The tectonostigraphic evolution of the Huronian basement and the subsequent basin fill: geological constraints on impact models of the Sudbury event. *Precambrian Res.* 129, 203–223.

Mathieu, L., van Wyk de Vries, B., 2009. Edifice and substrata deformation induced by intrusive complexes and gravitational loading in the Mull volcano (Scotland). *Bull. Volcanol.* 71. doi:10.1007/s00445-009-0295-5.

Mathieu, L., van Wyk de Vries, B., Holohan, E.P., Troll, V.R., 2008. Dykes, cups, saucers and sills: Analogue experiments on magma intrusion into brittle rocks. *Earth Planet. Sci. Lett.* 271. <https://doi.org/10.1016/j.epsl.2008.02.020>

Milkereit, B., Green, A., 1992. Deep geometry of the Sudbury structure from seismic reflection profiling. *Geology* 20, 807–811.

Morrison, G.G., 1984. Morphological features of the Sudbury structure in relation to an impact origin. *Geol. ore Depos. Sudbury Struct. Ed. by EG Pye, AJ Naldrett, PE Giblin. Ontario Geol. Surv. Spec.* 1, 513–520.

Mourre, G.A., 2000. Geological relationship at discontinuities in the Copper Cliff quartz diorite offset: an investigation into offset dikes and their relationship to the Sudbury Igneous Complex, Ontario Unpublished Master thesis University of Laurentia, Sudbury, ON, Canada.

Murphy, A.J., Spray, J.G., 2002. Geology, mineralization, and emplacement of the Whistle-Parkin offset dike, Sudbury. *Econ. Geol.* 97, 1399–1418.

Mytny, M., 2006. Structural review of the Copper Cliff South Mine. Report prepared for INCO Ltd

O’Callaghan, J.W., Osinski, G.R., Lightfoot, P.C., Linnen, R.L., Weirich, J.R., 2016. Reconstructing the geochemical signature of Sudbury breccia, Ontario, Canada: implications for its Formation and trace metal content. *Econ. Geol.* 111, 1705–1729.

Papapavlou, K., Darling, J.R., Lightfoot, P.C., Lasalle, S., Gibson, L., Storey, C.D., Moser, D., 2018. Polyorogenic reworking of ore controlling shear zones at the South Range of the Sudbury impact structure: a telltale story from in situ U-Pb titanite geochronology. *Terra* 254–261.

Papapavlou, K., Darling, J.R., Storey, C.D., Lightfoot, P.C., Moser, D.E., Lasalle, S., 2017. Dating shear zones with plastically deformed titanite: new insights into the orogenic evolution of the Sudbury impact structure (Ontario, Canada). *Precambrian Res.* 291, 220–235.

Pattison, E.F., 1979. The Sudbury sublayer. *Can. Mineral.* 17, 257–274.

Pilles, E.A., Osinski, G.R., Grieve, R.A.F., Smith, D., Bailey, J., 2018. Formation of large-scale impact melt dikes: a case study of the Foy Offset Dike at the Sudbury impact structure, Canada. *Earth Planet. Sci. Lett.* 495, 224–233.

Pilles, E.A., Osinski, G.R., Grieve, R.A.F., Smith, D.A., Bailey, J.M., 2017. Chemical variations and genetic relationships between the Hess and Foy offset dikes at the Sudbury impact structure. *Meteorit. Planet. Sci.* 52, 2647–2671.

Prevec, S.A., 2000. An examination of modal variation mechanisms in the contact sublayer of the Sudbury Igneous Complex, Canada. *Mineral. Petrol.* 68, 141–157.

Prevec, S.A., Büttner, S.H., 2018. Multiphase emplacement of impact melt sheet into the footwall: offset dykes of the Sudbury Igneous Complex, Canada. *Meteorit. Planet. Sci.* 53, 1301–1322.

Prevec, S.A., Cawthorn, R.G., 2002. Thermal evolution and interaction between impact melt sheet and footwall: a genetic model for the contact sublayer of the Sudbury Igneous Complex, Canada. *J. Geophys. Res. Solid Earth* 107, ECV-5.

Richardson, S.H., 1979. Chemical variation induced by flow differentiation in an extensive Karroo dolerite sheet, southern Namibia. *Geochim. Cosmochim. Acta* 43, 1433–1441.

Riller, U., 2005. Structural characteristics of the Sudbury impact structure, Canada: impact induced versus orogenic deformation-a review. *Meteorit. Planet. Sci.* 40, 1723–1740.

Riller, U., Boutelier, D., Schrank, C., Cruden, A.R., 2010a. Role of kilometer-scale weak circular heterogeneities on upper crustal deformation patterns: evidence from scaled analogue modeling and the Sudbury Basin, Canada. *Earth Planet. Sci. Lett.* 297, 587–597.

Riller, U., Clark, M.D., Daxberger, H., Doman, D., Lenauer, I., Plath, S., Santimano, T., 2017. Fault-slip inversions: their importance in terms of strain, heterogeneity, and kinematics of brittle deformation. *J. Struct. Geol.* 101, 80–95.

Riller, U., Lieger, D., Gibson, R.L., Grieve, R.A.F., Stöffler, D., 2010b. Origin of large-volume pseudotachylite in terrestrial impact structures. *Geology* 38, 619–622.

Riller, U., Schwerdtner, W.M., 1997. Mid-crustal deformation at the southern flank of the Sudbury Basin, central Ontario, Canada. *Geol. Soc. Am. Bull.* 109, 841–854.

Riller, U., Schwerdtner, W.M., Halls, H.C., Card, K.D., 1999. Transpressive tectonism in the eastern Penokean orogen, Canada: consequences for Proterozoic crustal kinematics and continental fragmentation. *Precambrian Res.* 93, 51–70.

Ripley, E.M., Lightfoot, P.C., Stifter, E.C., Underwood, B., Taranovic, V., Dunlop, M., III, Donoghue, K.A., 2015. Heterogeneity of S isotope compositions recorded in the Sudbury Igneous Complex, Canada: significance to formation of Ni-Cu sulfide ores and the host rocks. *Econ. Geol.* 110, 1125–1135.

Rousell, D.H., 1984. Structural geology of the Sudbury basin: Ontario Geological Survey Special.

Rousell, D.H., Brown, G.H., 2009. A field guide to the geology of Sudbury, Ontario. Ontario Ministry of Northern Development, Mines and Forestry

Rousell, D.H., Fedorowich, J.S., Dressler, B.O., 2003. Sudbury Breccia (Canada): a product of the 1850 Ma Sudbury Event and host to footwall Cu-Ni-PGE deposits. *Earth-Sci. Rev.* 60, 147–174.

Rousell, D.H., Long, D.G.F., 1998. Are outliers of the Huronian Supergroup preserved in structures associated with the collapse of the Sudbury Impact Crater? *J. Geol.* 106, 407–420.

Santimano, T., Riller, U., 2012. Revisiting thrusting, reverse faulting and transpression in the southern Sudbury Basin, Ontario. *Precambrian Res.* 200, 74–81.

Scott, R.G., Benn, K., 2002. Emplacement of sulfide deposits in the Copper Cliff offset dike during collapse of the Sudbury crater rim: evidence from magnetic fabric studies. *Econ. Geol.* 97, 1447–1458.

Scott, R.G., Spray, J.G., 2000. The South Range breccia belt of the Sudbury impact structure: a possible terrace collapse feature. *Meteorit. Planet. Sci.* 35, 505–520.

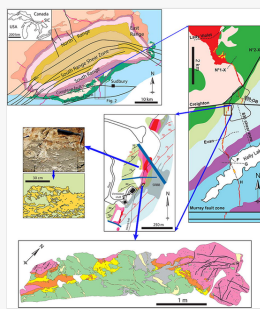
Shanks, W.S., 1991. Deformation of the central and southern portions of the Sudbury Structure Unpublished PhD thesis University of Toronto, Ontario.

Shanks, W.S., Schwerdtner, W.M., 1991a. Crude quantitative estimates of the original northwest-southeast dimension of the Sudbury Structure, south-central Canadian Shield. *Can. J. Earth Sci.* 28, 1677–1686.

Shanks, W.S., Schwerdtner, W.M., 1991b. Structural analysis of the central and southwestern Sudbury structure, Southern Province, Canadian Shield. *Can. J. Earth Sci.* 28, 411–430.

- Souch, B.E., Podolsky, T., Ltd., Gstinc., 1969. Geological Staff of the International Nickel Co. of Canada Ltd., 1969. The sulfide ores of Sudbury: Their particular relation to a distinctive inclusion--bearing facies of the Nickel Irruptive. *Econ. Geol.* 4, 252–261
- Speers, E.C., 1957. The age relation and origin of common Sudbury breccia. *J. Geol.* 65, 497–514.
- Therriault, A.M., Fowler, A.D., Grieve, R.A.F., 2002. The Sudbury igneous complex: a differentiated impact melt sheet. *Econ. Geol.* 97, 1521–1540.
- Thompson, L.M., Spray, J.G., 1994. Pseudotachylitic rock distribution and genesis within the Sudbury impact structure. *Spec. Pap. Soc. Am.* 275.
- Tschirhart, P., Morris, B., 2012. Grenville age deformation of the Sudbury impact structure: evidence from magnetic modelling of the Sudbury diabase dyke swarm. *Terra* 213–220.
- Wichman, R.W., Schultz, P.H., 1993. Floor fractured crater models of the Sudbury Structure, Canada: implications for initial crater size and crater modification. *Meteoritics* 28, 222–231.
- Wilkerson, M.S., Medwedeff, D.A., Marshak, S., 1991. Geometrical modeling of fault-related folds: a pseudo-three-dimensional approach. *J. Struct. Geol.* 13, 801–812.
- Wood, C.R., Spray, J.G., 1998. Origin and emplacement of offset dykes in the Sudbury impact structure: constraints from Hess. *Meteorit. Planet. Sci.* 33, 337–347.
- Yates, A.B., 1938. The Sudbury intrusive. *R. Soc. Canada Transcr.* 4, 151–172.
- Zieg, M.J., Marsh, B.D., 2005. The Sudbury Igneous Complex: viscous emulsion differentiation of a superheated impact melt sheet. *Geol. Soc. Am. Bull.* 117, 1427–1450.
- Zolnai, A.I., Price, R.A., Helmstaedt, H., 1984. Regional cross section of the Southern Province adjacent to Lake Huron, Ontario: implications for the tectonic significance of the Murray Fault Zone. *Can. J. Earth Sci.* 21, 447–456.

Graphical abstract



Highlights

- Melt movement and decoupling of silicate magma and sulfide melt revealed by field relationships.
- Downward melt migration into the Copper Cliff Offset (CCO) dyke, Sudbury Igneous Complex (SIC)
- Deformation facilitated through re-activation of E-W-striking pre-impact faults.

Appendix A Supplementary data

The following are the Supplementary data to this article:

[Multimedia Component 1](#)

Queries and Answers

Q1

Query: Your article is registered as a regular item and is being processed for inclusion in a regular issue of the journal. If this is NOT correct and your article belongs to a Special Issue/Collection please contact m.ayyamperumal@elsevier.com immediately prior to returning your corrections.

Answer: Yes

Q2

Query: The author names have been tagged as given names and surnames (surnames are highlighted in teal color). Please confirm if they have been identified correctly.

Answer: Yes

Q3

Query: Please note that as per standard style, a corresponding author footnote be provided for at least one author. Please check and assign the corresponding author name.

Answer: Lucie Mathieu (lucie1.mathieu@uqac.ca)